

# Double-Factor-Regularized Low-Rank Tensor Factorization for Mixed Noise Removal in Hyperspectral Image

Yu-Bang Zheng<sup>ID</sup>, *Student Member, IEEE*, Ting-Zhu Huang<sup>ID</sup>, Xi-Le Zhao<sup>ID</sup>,  
Yong Chen<sup>ID</sup>, and Wei He<sup>ID</sup>, *Member, IEEE*

**Abstract**—As a preprocessing step, hyperspectral image (HSI) restoration plays a critical role in many subsequent applications. Recently, based on the framework of subspace representation and low-rank matrix/tensor factorization (LRMF/LRTF), many single-factor-regularized methods add various regularizations on the spatial factor to characterize its spatial prior knowledge. However, these methods neglect the common characteristics among different bands and the spectral continuity of HSIs. To tackle this issue, this article establishes a bridge between the factor-based regularization and the HSI priors and proposes a double-factor-regularized LRTF model for HSI mixed noise removal. The proposed model employs LRTF to characterize the spectral global low rankness, introduces a weighted group sparsity constraint on the spatial difference images (SpatDIs) of the spatial factor to promote the group sparsity in the SpatDIs of HSIs, and suggests a continuity constraint on the spectral factor to promote the spectral continuity of HSIs. Moreover, we develop a proximal alternating minimization-based algorithm to solve the proposed model. Extensive experiments conducted on the simulated and real HSIs demonstrate that the proposed method has superior performance on mixed noise removal compared with the state-of-the-art methods based on subspace representation, noise modeling, and LRMF/LRTF.

**Index Terms**—Factor-based regularization (FR), hyperspectral image (HSI), low-rank tensor factorization (LRTF), mixed noise removal, proximal alternating minimization (PAM).

## I. INTRODUCTION

HYPERSPECTRAL images (HSIs) reflect different imaging effects of one real scene under hundreds of contiguous spectral bands. Compared with gray-scale images, HSIs contain a wealth of spatial and spectral information, making them widely applied in various applications [1], such

Manuscript received January 13, 2020; revised March 17, 2020; accepted April 10, 2020. This work was supported in part by the National Natural Science Foundation of China under Grant 61772003 and Grant 61876203 and in part by the Japan Society for the Promotion of Science under Grant KAKENHI 19K20308. (Corresponding authors: Ting-Zhu Huang; Xi-Le Zhao.)

Yu-Bang Zheng, Ting-Zhu Huang, Xi-Le Zhao, and Yong Chen are with the Research Center for Image and Vision Computing, School of Mathematical Sciences, University of Electronic Science and Technology of China, Chengdu 611731, China (e-mail: zhengyubang@163.com; tingzhuhuang@126.com; xlzhao122003@163.com; chenyong1872008@163.com).

Wei He is with the Geoinformatics Unit, RIKEN Center for Advanced Intelligence Project, RIKEN, Tokyo 103-0027, Japan (e-mail: wei.he@riken.jp).

Color versions of one or more of the figures in this article are available online at <http://ieeexplore.ieee.org>.

Digital Object Identifier 10.1109/TGRS.2020.2987954

as natural disaster monitoring, terrain detection, and land use analysis. Unfortunately, real-world HSIs always suffered from all sorts of noise, including the Gaussian noise, salt and pepper noise, deadlines, and stripes. The existence of the abovementioned noise greatly reduces the quality of HSIs, resulting in the infeasibility of subsequent applications, such as classification [2]–[4], unmixing [5]–[7], fusion [8], and target detection [9]. Hence, restoring the clean HSI from a noisy observation, i.e., HSI restoration, plays a critical role in HSI applications. Deeply exploring and accurately describing the spatial and spectral knowledge in HSIs are the core issues of HSI restoration. Among the currently HSI restoration methods, low rankness, local continuity, and nonlocal self-similarity are the most frequently researched HSI priors [10]–[23].

Since each band of HSIs can be regarded as a gray-scale image, the simplest and most direct way for HSI restoration is to employ the traditional gray-scale image restoration methods, such as NLM [24], K-SVD [25], BM3D [26], and WNNM [27], to restore the target HSI band-by-band. However, the most shortcoming of this kind of method is the neglect of the spectral correlations, which is crucial prior knowledge for improving the performance of HSI restoration. Consequently, a variety of efficient methods have been introduced to simultaneously consider spatial and spectral prior, leading to a great improvement in restoring results. For example, to consider spatial information and spectral noise differences simultaneously, Yuan *et al.* [28] introduced a spectral–spatial adaptive total variation (TV) to HSI restoration and obtained a promising result. By supposing that the first several components output by the principal component analysis (PCA) contain the major information of images, Chen and Qian [29] proposed an HSI restoration method, which first performs PCA on the noisy HSI, then employs the bivariate wavelet thresholding and a wavelet transform algorithm to remove the noise in the last several components, and finally obtains the restored HSI via inverse PCA. Besides, to exploit nonlocal self-similarity in both spatial and spectral domains, many restoration methods regarded the group of similar 3-D cubes as the basic unit for restoring. Examples include non-local groupwise spectrum-PCA [30], nonlocal tensor dictionary learning [31], and nonlocal tensor ring decomposition [32]. To utilize the spectral global low rankness and spatial

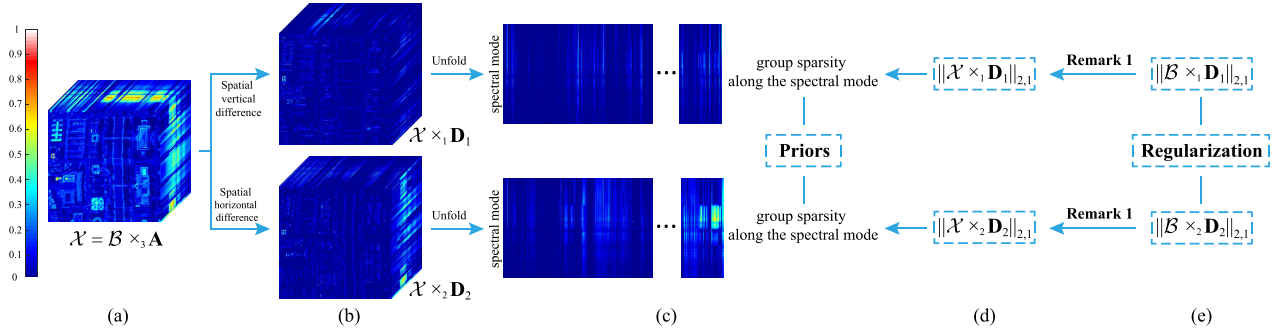


Fig. 1. Group sparsity along the spectral mode of the spatial difference images and the proposed regularization terms based on the spatial factor  $\mathcal{B}$ . (a) HSI Washington DC Mall  $\mathcal{X} \in \mathbb{R}^{256 \times 256 \times 170}$ , which can be factorized as  $\mathcal{B} \times_3 \mathbf{A}$ , where  $\mathcal{B} \in \mathbb{R}^{256 \times 256 \times r}$ ,  $\mathbf{A} \in \mathbb{R}^{170 \times r}$ , and  $r \ll 170$ . (b) Images obtained by performing spatial difference operators, where  $\mathbf{D}_1$  and  $\mathbf{D}_2$  are the first-order difference matrixes. (c) Mode-3 unfolding matrices of the corresponding difference images. (d) Regularization terms on the original HSI  $\mathcal{X}$  used to promote the group sparsity. (e) Regularization terms on the factor  $\mathcal{B}$  used to replace the regularization terms on the original HSI  $\mathcal{X}$ .

nonlocal self-similarity, under the framework of subspace representation, Zhuang and Bioucas-Dias [33] employed the BM3D to eigen images denoising, and He *et al.* [34] embedded the WNNM to eigenimages denoising while updating the subspace iteratively. However, the aforementioned methods only focus on removing one type of noise, especially the Gaussian noise. However, in most realistic scenarios, the noise in HSIs usually manifests as a mixture of several kinds of noise.

Recently, an increasing number of researchers have been putting great effort into mixed noise removal to adapt to real noise situations. Based on the low-rankness prior hypothesis, Zhang *et al.* [35] made the first attempt to employ low-rank matrix recovery (LRMR)-based framework to remove the mixed noise. Specifically, this method first separates the noisy HSI as overlapped full-band 3-D cubes, then unfolds 3-D cubes to matrices along the spectral mode, and finally uses the LRMR-based framework to restore unfolding matrices. Consequently, to enhance the performance of LRMR, a series of low-rank matrix approximation (LRMA)-based methods introduced nonconvex functions to approximate the rank of the unfolded HSIs [36], [37]. However, LRMA-based methods involve the singular value decomposition (SVD), leading to high computational complexity. To tackle this issue, low-rank matrix factorization (LRMF) is used to the HSI mixed noise removal problem with several flexible noise distributions hypothesis, such as a mixture of independent and identically distributed (i.i.d.) exponential power distributions [38] and a mixture of non-i.i.d. Gaussian distributions [39]. By regarding HSIs as third-order tensors, a large number of methods used the tensor decompositions/tensor rank minimization, such as the Tucker decomposition [40], [41], PARAFAC decomposition [42], and tensor-SVD [43], [44], to exploit the global low rankness of HSIs. Among them, Fan *et al.* [43] assumed that the clean HSI is a low-tubal-rank part and introduced an HSI mixed noise removal model by minimizing the convex relaxation of the tubal rank. Zheng *et al.* [44] subsequently proposed a new tensor rank, i.e., tensor fibered rank, to more flexibly and accurately explore the low rankness of HSIs, achieving a great improvement in mixed noise removal. However, most of the aforementioned methods only considered the

low rankness and, thus, cannot to exhaust the intrinsic potential of HSIs, leading to a room for further enhancement.

To further boost the denoising performance, many researchers proposed a variety of HSI mixed noise removal models based on the framework of the convolutional neural network (CNN) [45]–[48], which has the powerful nonlinear fitting and feature expression ability. For example, Chang *et al.* [45] proposed a CNN-based method by modeling the spatial and the spectral features by the dilated convolution and multichannel filters, respectively. Zhang *et al.* [46] introduced a method based on the spatial–spectral gradient network, which is capable of extracting the directional feature of sparse noise and exploring abundant spectral information of HSIs. Meanwhile, many methods considered not only the low-rankness prior but also the local continuity and nonlocal self-similarity priors. For example, He *et al.* [49] proposed a method, which employed LRMF to explore the spectral low rankness while applying the spatial TV to each band of HSIs to exploit the spatial local continuity. To further take the spectral local continuity into consideration, the spatial–spectral TV has been proposed and integrated into various low-rank-based models, such as weighted nuclear norm [50] and low-rank Tucker decomposition (LRTD) [51], [52]. Besides, Chen *et al.* [53] conducted a group sparsity regularization on spatial difference images under the framework of LRTD, obtaining a promising result. However, the regularization terms in the aforementioned methods were added to HSIs, resulting in high computational complexity.

To reduce the computational complexity, several single-factor-regularized methods have been proposed based on the framework of LRMF/low-rank tensor factorization (LRTF) [54]–[56]. Specifically, an HSI  $\mathcal{X} \in \mathbb{R}^{n_1 \times n_2 \times n_3}$  can be factorized as  $\mathcal{X} = \mathcal{B} \times_3 \mathbf{A}$ , where  $\mathbf{A} \in \mathbb{R}^{n_3 \times r}$  and  $\mathcal{B} \in \mathbb{R}^{n_1 \times n_2 \times r}$  ( $r \ll n_3$ ) denote the spectral factor and the spatial factor, respectively. The existing methods usually regarded each frontal slice of the spatial factor  $\mathcal{B}$  as a gray-scale image and, subsequently, used various regularization to explore its prior. Examples include the TV/framelet-regularization used to explore the spatial local continuity [54], [55] and the nonlocal low-rank regularization used to exploit the spatial nonlocal self-similarity [56]. However, there are still exist two

issues. On the one hand, these methods cannot fully explore the common characteristics, except the global low rankness, of different bands. For example, most of the smooth areas in different bands of an HSI usually located at the same location since different bands present the same scene. This common characteristic causes the spatial difference images (SpatDIs) of the HSIs, as shown in Fig. 1(b) and (c), to be group sparse along the spectral mode.<sup>1</sup> On the other hand, these methods neglect the local continuity along the spectral mode of HSIs.

In this article, we propose a double-factor-regularized LRTF (LRTF-DFR) method for HSI mixed noise removal, which not only employs the LRTF framework  $\mathcal{X} = \mathcal{B} \times_3 \mathbf{A}$  to characterize the spectral global low rankness of HSIs but also utilizes the regularization terms on the spatial factor  $\mathcal{B}$  and the spectral factor  $\mathbf{A}$  to depict the aforementioned group sparsity and spectral continuity, respectively. The contributions of this article are mainly the following three aspects.

First, a direct way to explore aforementioned group sparsity is to utilize the  $\ell_{2,1}$ -norm on the SpatDIs of HSIs, i.e.,  $\|\mathcal{X} \times_k \mathbf{D}_k\|_{2,1}$  ( $k = 1, 2$ ) shown in Fig. 1(d). Instead of this direct way, this article unitizes the  $\ell_{2,1}$ -norm on the SpatDIs of the spatial factor  $\mathcal{B}$ , i.e.,  $\|\mathcal{B} \times_k \mathbf{D}_k\|_{2,1}$  shown in Fig. 1(e), and proves that  $\mathcal{X} \times_k \mathbf{D}_k$  must be group sparse along the spectral mode when  $\mathcal{B} \times_k \mathbf{D}_k$  is group sparse along the third mode. Meanwhile, a weighted strategy is employed to better promote the group sparsity.

Second, we note that each spectral vector (tube) of an HSI  $\mathcal{X}$  can be mathematically expressed as the linear combination of all column of the spectral factor  $\mathbf{A}$ , i.e., columns of  $\mathbf{A}$  can be regarded as a basis of the spectral space of  $\mathcal{X}$ . Since continuous bases tend to generate continuous data, this article promotes the continuity of spectral vectors of  $\mathcal{X}$  by boosting the continuity of columns of  $\mathbf{A}$ .

Third, an efficient proximal alternating minimization [57] (PAM)-based algorithm is developed to solve the proposed LRTF-DFR method. Extensive experiments conducted on simulated and real HSIs exhibit the superior performance of the proposed LRTF-DFR on mixed noise removal, spatial image recovery, and spectral signatures preserving compared with several excellent methods.

The rest of this article is organized as follows. Section II gives some notations and preliminary knowledge. Section III presents the proposed LRTF-DFR-based HSI restoration model and develops a PAM-based solving algorithm with a detailed computational complexity analysis. Section IV carries out extensive experiments to illustrate the superiority of the proposed model. Section V summarizes this article.

## II. NOTATIONS AND PRELIMINARIES

Following the nomenclatures of [58], we summarize notations used in this article in Table I. Next, we introduce the definitions of mode- $k$  unfolding, mode- $k$  tensor-matrix product, and the Tucker rank.

**Definition 1 (Mode- $k$  Unfolding):** For an  $N$ th-order tensor  $\mathcal{X} \in \mathbb{R}^{n_1 \times n_2 \times \cdots \times n_N}$ , its mode- $k$  unfolding  $\mathbf{X}_{(k)}$  is an  $n_k \times$

<sup>1</sup>The number of spectral vectors whose elements are approximately all zero is much more than that of the nonzero ones.

TABLE I  
NOTATION DECLARATIONS

Notations	Interpretations
$x, \mathbf{x}, \mathbf{X}, \mathcal{X}$	scalar, vector, matrix, tensor
$x_{i_1, i_2, \dots, i_N}$ or $\mathcal{X}(i_1, i_2, \dots, i_N)$	the $(i_1, i_2, \dots, i_N)$ th element of $\mathcal{X}$
$\mathbf{x}_{:, i_2, i_3}$ or $\mathcal{X}(:, i_2, i_3)$	the $(i_2, i_3)$ th column of a third-order tensor $\mathcal{X}$
$\mathbf{x}_{i_1, :, i_3}$ or $\mathcal{X}(i_1, :, i_3)$	the $(i_1, i_3)$ th row of a third-order tensor $\mathcal{X}$
$\mathbf{x}_{i_1, i_2, :}$ or $\mathcal{X}(i_1, i_2, :)$	the $(i_1, i_2)$ th tubal of a third-order tensor $\mathcal{X}$
$\ \mathcal{X}\ _F$	Frobenius norm
$\ \mathcal{X}\ _F$	$\ \mathcal{X}\ _F = \sqrt{\sum_{i_1, i_2, \dots, i_N}  x_{i_1, i_2, \dots, i_N} ^2}$
$\ \mathcal{X}\ _1$	$\ell_1$ -norm
$\ \mathcal{X}\ _{2,1}$	$\ell_{2,1}$ -norm of third-order tensors
$\mathbf{X}_{(k)}$	$\ \mathcal{X}\ _{2,1} = \sum_{i_1, i_2}  x_{i_1, i_2, :} _2$
$\langle \cdot, \cdot \rangle$	the mode- $k$ unfolding of $\mathcal{X}$
$\otimes$	inner product
$\odot$	Kronecker product
$\oslash$	component-wise multiplication
$\times_k$	component-wise division
	mode- $k$ tensor-matrix product

$\prod_{i \neq k} n_i$  matrix, which satisfies that  $\mathbf{X}_{(k)}(i_k, j)$  is mapped by  $\mathcal{X}(i_1, i_2, \dots, i_N)$ , where  $j = 1 + \sum_{s=1, s \neq k}^N (i_s - 1) J_s$  with  $J_s = \sum_{m=1, m \neq k}^{s-1} n_m$ . The corresponding operator and inverse operator are denoted as  $\mathbf{X}_{(k)} = \text{Unfold}_k(\mathcal{X})$  and  $\mathcal{X} = \text{Fold}_k(\mathbf{X}_{(k)})$ , respectively.

**Definition 2 (Mode- $k$  Tensor-Matrix Product):** The mode- $k$  tensor-matrix product of an  $n_1 \times n_2 \times \cdots \times n_N$  tensor  $\mathcal{X}$  and a  $J \times n_k$  matrix  $\mathbf{A}$  is an  $n_1 \times \cdots \times n_{k-1} \times J \times n_{k+1} \times \cdots \times n_N$  tensor denoted by  $\mathcal{X} \times_k \mathbf{A}$  and satisfied

$$(\mathcal{X} \times_k \mathbf{A})_{i_1, \dots, i_{k-1}, j, i_{k+1}, \dots, i_N} = \sum_{i_k=1}^{n_k} x_{i_1, i_2, \dots, i_N} \cdot a_{j, i_k}.$$

According to abovementioned two definitions, we have

$$\mathcal{Y} = \mathcal{X} \times_k \mathbf{A} \Leftrightarrow \mathbf{Y}_{(k)} = \mathbf{A} \mathbf{X}_{(k)}$$

and

$$\begin{aligned} \mathcal{Y} &= \mathcal{X} \times_1 \mathbf{A}_1 \times_2 \mathbf{A}_2 \cdots \times_N \mathbf{A}_N \Leftrightarrow \\ \mathbf{Y}_{(k)} &= \mathbf{A}_k \mathbf{X}_{(k)} (\mathbf{A}_N \otimes \cdots \otimes \mathbf{A}_{k+1} \otimes \mathbf{A}_{k-1} \otimes \cdots \otimes \mathbf{A}_1)^T. \end{aligned}$$

**Definition 3 (Tucker Rank):** For an  $N$ th-order tensor  $\mathcal{X} \in \mathbb{R}^{n_1 \times n_2 \times \cdots \times n_N}$ , its Tucker rank is defined as

$$\text{Rank}_T(\mathcal{X}) = (\text{Rank}(\mathbf{X}_{(1)}), \text{Rank}(\mathbf{X}_{(2)}), \dots, \text{Rank}(\mathbf{X}_{(N)})).$$

Interested readers can obtain a more detailed introduction for tensors in [58].

## III. PROPOSED HSI RESTORATION MODEL AND SOLVING ALGORITHM

### A. Problem Formulation and Motivation

By simply assuming that the noisy HSI  $\mathcal{Y} \in \mathbb{R}^{n_1 \times n_2 \times n_3}$  is corrupted by the additive Gaussian noise  $\mathcal{N}$  and the additive sparse noise  $\mathcal{S}$  (salt and pepper noise, deadlines, and stripes), the HSI degradation formulation can be expressed as

$$\mathcal{Y} = \mathcal{X} + \mathcal{N} + \mathcal{S}.$$

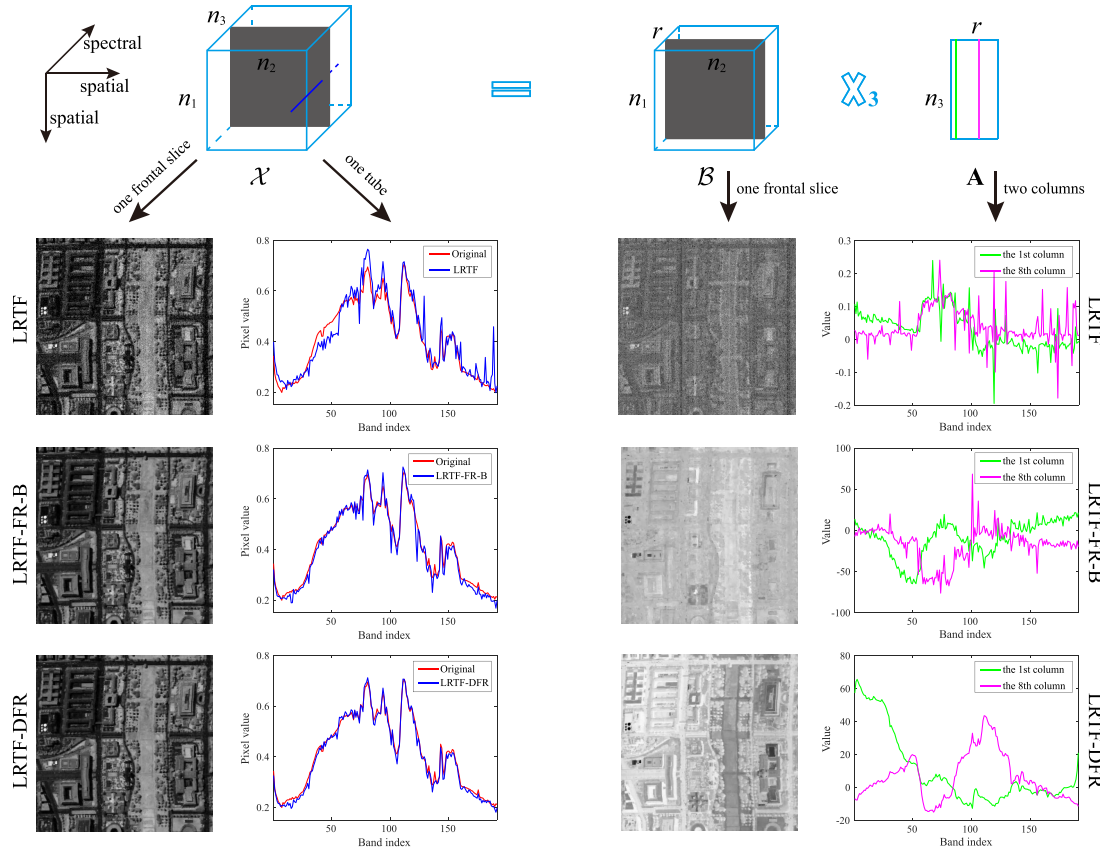


Fig. 2. Impact of each term in the proposed LRTF-DFR on the performance of HSI restoration. From the second to fourth rows: the results of the method without factor-based regularization (LRTF), the method only with factor  $\mathcal{B}$ -based regularization (LRTF-FR-B), and the proposed LRTF-DFR, respectively. (From Left to Right) Restoration results at band 72, restoration results of the spectral vector at spatial location (150, 150), one frontal slice of the spatial factor  $\mathcal{B}$ , and two columns of the spectral factor  $\mathbf{A}$ .

The key issue of recovering the clean HSI  $\mathcal{X}$  from  $\mathcal{Y}$  is to exactly characterize the HSI prior by establishing appropriate regularization terms. Mathematically, a generalized HSI restoration model can be formulated as

$$\min_{\mathcal{X}, \mathcal{S}} \frac{1}{2} \|\mathcal{Y} - \mathcal{X} - \mathcal{S}\|_F^2 + \tau \mathcal{R}(\mathcal{X}) + \mu \|\mathcal{S}\|_1 \quad (1)$$

where  $\tau$  and  $\mu$  are regularization parameters;  $\mathcal{R}(\mathcal{X})$  is the regularization term designed to exploit the HSI prior. For example,  $\mathcal{R}(\mathcal{X})$  was designed as the tensor nuclear norm [43], [44] and the Schatten  $p$ -norm [36] to explore low-rankness prior, spatial-spectral TV [52] and enhanced 3-D TV [59] to characterize spatial-spectral continuity prior, and nonlocal low-rank regularization [51] to exploit nonlocal self-similarity prior. However, adding regularization on HSIs will inevitably lead to high computational complexity since HSIs usually have a large scale.

Fortunately, the spectral low rankness of HSIs can be represented as the mode-3 tensor-matrix product of a low-dimensional tensor and a low-dimensional matrix, i.e., the clean HSI  $\mathcal{X}$  can be approximately factorized as

$$\mathcal{X} = \mathcal{B} \times_3 \mathbf{A} \quad (2)$$

where  $\mathcal{B} \in \mathbb{R}^{n_1 \times n_2 \times r}$  ( $r \ll n_3$ ) denotes the spatial factor and  $\mathbf{A} \in \mathbb{R}^{n_3 \times r}$  represents the spectral factor. Since the spatial factor  $\mathcal{B}$  usually reflects the spatial characteristics of HSIs [33], [34], many subspace-based and LRMF/LRTF-based methods

employed various regularization on  $\mathcal{B}$ , and their models can be generally formulated as

$$\min_{\mathbf{A}, \mathcal{B}, \mathcal{S}} \frac{1}{2} \|\mathcal{Y} - \mathcal{B} \times_3 \mathbf{A} - \mathcal{S}\|_F^2 + \tau \mathcal{R}(\mathcal{B}) + \mu \|\mathcal{S}\|_1 \quad (3)$$

where  $\mathbf{A}$  satisfies  $\mathbf{A}^T \mathbf{A} = \mathbf{I}$  in subspace-based methods and  $\mathcal{R}(\mathcal{B})$  is the regularization term designed to exploit its prior. For example,  $\mathcal{R}(\mathcal{B})$  was designed as the framelet-regularization [55] and nonlocal low-rank regularization [56] to explore the spatial local continuity and the spatial nonlocal self-similarity, respectively. However, the existing regularization on  $\mathcal{B}$  cannot fully explore the common characteristics among different bands of HSIs, such as the spectral group sparsity in SpatDIS of HSIs. Meanwhile, the spectral continuity of HSIs was also neglected.

### B. LRTF-DFR-Based HSI Restoration Model

To consider the aforementioned spectral group sparsity and spectral continuity in the HSI  $\mathcal{X}$ , we introduce regularization on factors in (2) and propose an LRTF-DFR-based HSI restoration method as follows:

$$\begin{aligned} \min_{\mathbf{A}, \mathcal{B}, \mathcal{S}} & \frac{1}{2} \|\mathcal{Y} - \mathcal{B} \times_3 \mathbf{A} - \mathcal{S}\|_F^2 + \tau \sum_{k=1}^2 \|\mathcal{W}_k \odot (\mathcal{B} \times_k \mathbf{D}_k)\|_{2,1} \\ & + \lambda \|\mathbf{D}_3 \mathbf{A}\|_F^2 + \mu \|\mathcal{W}_s \odot \mathcal{S}\|_1 \end{aligned} \quad (4)$$

where  $\tau$ ,  $\lambda$ , and  $\mu$  are regularization parameters;  $\mathbf{D}_k$  ( $k = 1, 2, 3$ ) are first-order difference matrices; and  $\mathcal{W}_k$  ( $k = 1, 2$ ) and  $\mathcal{W}_s$  are weight tensors used to better promote the group sparsity [53] and the sparsity [60], respectively. Especially, all frontal slices of  $\mathcal{W}_k$  are the same matrices, denoted as  $\mathbf{W}_k$ . Most importantly, Remarks 1 and 2 give a detail illustration of why the group sparsity constraint on  $\mathcal{B} \times_k \mathbf{D}_k$  ( $k = 1, 2$ ) can promote the group sparsity in  $\mathcal{X} \times_k \mathbf{D}_k$  and the continuity constraint on  $\mathbf{A}$  can promote the spectral continuity of  $\mathcal{X}$ .

*Remark 1 (Factor  $\mathcal{B}$ -Based Regularization):* With Definition 2, we have

$$\begin{aligned}\mathcal{X} \times_k \mathbf{D}_k &= (\mathcal{B} \times_3 \mathbf{A}) \times_k \mathbf{D}_k = (\mathcal{B} \times_k \mathbf{D}_k) \times_3 \mathbf{A} \\ &\Leftrightarrow [\mathcal{X} \times_k \mathbf{D}_k](i, j, :) = \sum_{t=1}^r [\mathcal{B} \times_k \mathbf{D}_k](i, j, t) \mathbf{A}(:, t).\end{aligned}$$

It can be easy to obtain that  $[\mathcal{X} \times_k \mathbf{D}_k](i, j, :) = 0$  when  $[\mathcal{B} \times_k \mathbf{D}_k](i, j, :) = 0$ . Therefore, when  $\mathcal{B} \times_k \mathbf{D}_k$  is group sparse along the third mode,  $\mathcal{X} \times_k \mathbf{D}_k$  must be group sparse along the third (spectral) mode. Moreover, the abovementioned conclusion is also true in reverse. This is because  $[\mathcal{B} \times_k \mathbf{D}_k](i, j, :) = 0$  when  $[\mathcal{X} \times_k \mathbf{D}_k](i, j, :) = 0$  since  $\mathbf{A}(:, 1)$ ,  $\mathbf{A}(:, 2)$ , ..., and  $\mathbf{A}(:, r)$  are linearly independent.

*Remark 2 (Factor  $\mathbf{A}$ -Based Regularization):* By rewriting  $\mathcal{X} = \mathcal{B} \times_3 \mathbf{A}$  as  $\mathbf{X}_{(3)} = \mathbf{AB}_{(3)}$ , it is not hard to find that each spectral vector of  $\mathcal{X}$  (column of  $\mathbf{X}_{(3)}$ ) can be mathematically expressed as a linear combination of all column of the spectral factor  $\mathbf{A}$ . This implies that columns of  $\mathbf{A}$  can be regarded as a basis of the spectral space of  $\mathcal{X}$ . Since continuous bases usually tend to generate continuous data, boosting the continuity of the columns of  $\mathbf{A}$  can promote the continuity of the spectral vector of  $\mathcal{X}$  compared with the case without the continuity constraint.

We take an example shown in Fig. 2 to illustrate the impact of the factor-based regularization terms in the proposed LRTF-DFR on the performance of mixed noise removal. By comparing the second and third rows, we find that due to the group sparsity constraint on  $\mathcal{B} \times_k \mathbf{D}_k$  ( $k = 1, 2$ ), the frontal slice of  $\mathcal{B}$  obtained by LRTF-FR-B contains more geometrical features than that obtained by LRTF, leading to a significant improvement in HSI restoration. By comparing the third and fourth rows, we find that due to the column continuity constraint on  $\mathbf{A}$ , the spectral vector obtained by the proposed LRTF-DFR is much smoother and closer to the original ones than that by LRTF-FR-B. The abovementioned observations empirically illustrate the significance of the factor-based regularization terms and consistent with the previous theoretical discussions.

In summary, the proposed LRTF-DFR has the following two advantages.

### 1) Double-Factor-Based Regularization for HSI Prior:

Compared with the single-factor-regularized methods [54]–[56], the proposed LRTF-DFR explores more HSI prior knowledge in both spatial and spectral domains since both spatial and spectral factors are fully utilized.

### 2) Lower Computational Complexity:

Compared with the method using regularization on the original HSI [52], [53], the proposed LRTF-DFR has lower computational

complexity since the scales of factors are much smaller than that of the original HSI.

### C. PAM-Based Solving Algorithm

Within the framework of PAM-based algorithm, the problem (4) can be solved by alternately updating

$$\begin{cases} \text{Step 1: } \mathbf{A}^{l+1} = \underset{\mathbf{A}}{\operatorname{argmin}} f(\mathbf{A}, \mathcal{B}^l, \mathcal{S}^l) + \frac{\rho}{2} \|\mathbf{A} - \mathbf{A}^l\|_F^2 \\ \text{Step 2: } \mathcal{B}^{l+1} = \underset{\mathcal{B}}{\operatorname{argmin}} f(\mathbf{A}^{l+1}, \mathcal{B}, \mathcal{S}^l) + \frac{\rho}{2} \|\mathcal{B} - \mathcal{B}^l\|_F^2 \\ \text{Step 3: } \mathcal{S}^{l+1} = \underset{\mathcal{S}}{\operatorname{argmin}} f(\mathbf{A}^{l+1}, \mathcal{B}^{l+1}, \mathcal{S}) + \frac{\rho}{2} \|\mathcal{S} - \mathcal{S}^l\|_F^2 \end{cases} \quad (5)$$

where  $f(\mathbf{A}, \mathcal{B}, \mathcal{S})$  is the objective function of (4) and  $\rho > 0$  is the proximal parameter.

1) *Update  $\mathbf{A}$ :* In Step 1 of (5), the  $\mathbf{A}$ -subproblem is as follows:

$$\begin{aligned}\underset{\mathbf{A}}{\operatorname{argmin}} \frac{1}{2} \|\mathcal{Y} - \mathcal{B}^l \times_3 \mathbf{A} - \mathcal{S}^l\|_F^2 \\ + \lambda \|\mathbf{D}_3 \mathbf{A}\|_F^2 + \frac{\rho}{2} \|\mathbf{A} - \mathbf{A}^l\|_F^2\end{aligned} \quad (6)$$

whose solver can be directly obtained by solving the following Sylvester matrix equation:

$$\begin{aligned}\mathbf{AB}_{(3)}^l (\mathbf{B}_{(3)}^l)^T + 2\lambda \mathbf{D}_3^T \mathbf{D}_3 \mathbf{A} + \rho \mathbf{A} \\ = (\mathbf{Y}_{(3)} - \mathbf{S}_{(3)}^l) (\mathbf{B}_{(3)}^l)^T + \rho \mathbf{A}^l.\end{aligned} \quad (7)$$

To efficiently solve (7), we introduce the following theorem.

*Theorem 1 (Fast Solution of Sylvester Matrix Equation):* Suppose that  $\mathbf{A} \in \mathbb{R}^{m \times m}$ ,  $\mathbf{B} \in \mathbb{R}^{n \times n}$ , and  $\mathbf{X}, \mathbf{Y} \in \mathbb{R}^{m \times n}$ . The classical Sylvester matrix equation

$$\mathbf{AX} + \mathbf{XB} = \mathbf{Y}$$

has a unique solution if only if  $\mathbf{I}_n \otimes \mathbf{A} + \mathbf{B}^T \otimes \mathbf{I}_m$  is a invertible matrix. Especially, if

$$\mathbf{A} = \mathbf{U}_1 \Lambda_1 \mathbf{U}_1^T \text{ and } \mathbf{B} = \mathbf{U}_2 \Lambda_2 \mathbf{U}_2^T$$

this unique solution can be expressed as

$$\mathbf{X} = \mathbf{U}_1 ((1 \otimes \mathbf{T}) \odot (\mathbf{U}_1^T \mathbf{Y} \mathbf{U}_2)) \mathbf{U}_2^T$$

where  $\Lambda_1$  and  $\Lambda_2$  are diagonal matrices,  $\mathbf{U}_1$  and  $\mathbf{U}_2$  are unitary matrices, and

$$\begin{aligned}\mathbf{T} = (\operatorname{diag}^2(\Lambda_1), \operatorname{diag}(\Lambda_1), \dots, \operatorname{diag}(\Lambda_1)) \\ + (\operatorname{diag}(\Lambda_2), \operatorname{diag}(\Lambda_2), \dots, \operatorname{diag}(\Lambda_2))^T.\end{aligned}$$

In (7), it is not hard to find that the matrix  $\mathbf{D}_3^T \mathbf{D}_3$  is a circulant matrix and the matrix  $\mathbf{B}_{(3)}^l (\mathbf{B}_{(3)}^l)^T$  is a symmetric matrix. Therefore, we utilize 1-D fast Fourier transformation (FFT) and SVD to diagonalize  $\mathbf{D}_3^T \mathbf{D}_3$  and  $\mathbf{B}_{(3)}^l (\mathbf{B}_{(3)}^l)^T$ , respectively. That is

$$\mathbf{D}_3^T \mathbf{D}_3 = \mathbf{F}_1^T \Psi_1 \mathbf{F}_1 \text{ and } \mathbf{B}_{(3)}^l (\mathbf{B}_{(3)}^l)^T = \mathbf{U}_1 \Sigma_1 \mathbf{U}_1^T$$

where  $\mathbf{F}_1$  is 1-D discrete Fourier transformation (DFT) matrix. By using Theorem 1, we can efficiently solve (7) as

$$\mathbf{A}^{l+1} = \mathbf{F}_1^T ((1 \otimes \mathbf{T}_1) \odot (\mathbf{F}_1 \mathbf{G} \mathbf{U}_1)) \mathbf{U}_1^T \quad (8)$$

<sup>2</sup> $\operatorname{diag}(\Lambda)$  is a column vector whose elements are diagonal elements of  $\Lambda$ .

where  $\mathbf{G} = (\mathbf{Y}_{(3)} - \mathbf{S}_{(3)}^l)(\mathbf{B}_{(3)}^l)^T + \rho \mathbf{A}^l$  and

$$\begin{aligned} \mathbf{T}_1 &= 2\lambda(\text{diag}(\Psi_1), \text{diag}(\Psi_1), \dots, \text{diag}(\Psi_1)) + \rho \text{ones}^3(n_3, r) \\ &\quad + (\text{diag}(\Sigma_1), \text{diag}(\Sigma_1), \dots, \text{diag}(\Sigma_1))^T. \end{aligned}$$

2) *Update  $\mathcal{B}$ :* In Step 2 of (5), the  $\mathcal{B}$ -subproblem is as follows:

$$\begin{aligned} \underset{\mathcal{B}}{\text{argmin}} \quad & \frac{1}{2} \|\mathcal{Y} - \mathcal{B} \times_3 \mathbf{A}^{l+1} - \mathcal{S}^l\|_F^2 \\ & + \tau \sum_{k=1}^2 \|\mathcal{W}_k \odot (\mathcal{B} \times_k \mathbf{D}_k)\|_{2,1} + \frac{\rho}{2} \|\mathcal{B} - \mathcal{B}^l\|_F^2. \end{aligned} \quad (9)$$

We use the alternating direction method of multipliers (ADMM) [61] to solve (9). By introducing two auxiliary variables  $\mathcal{Z}_1$  and  $\mathcal{Z}_2$ , we rewrite (9) as

$$\begin{aligned} \underset{\mathcal{B}, \mathcal{Z}_1, \mathcal{Z}_2}{\text{argmin}} \quad & \frac{1}{2} \|\mathcal{Y} - \mathcal{B} \times_3 \mathbf{A}^{l+1} - \mathcal{S}^l\|_F^2 \\ & + \tau \sum_{k=1}^2 \|\mathcal{W}_k \odot \mathcal{Z}_k\|_{2,1} + \frac{\rho}{2} \|\mathcal{B} - \mathcal{B}^l\|_F^2 \\ \text{s.t. } & \mathcal{B} \times_k \mathbf{D}_k = \mathcal{Z}_k, \quad k = 1, 2. \end{aligned} \quad (10)$$

The augmented Lagrangian function of (10) is

$$\begin{aligned} L_\beta(\mathcal{B}, \mathcal{Z}_k, \mathcal{P}_k) &= \frac{1}{2} \|\mathcal{Y} - \mathcal{B} \times_3 \mathbf{A}^{l+1} - \mathcal{S}^l\|_F^2 \\ & + \sum_{k=1}^2 \left\{ \tau \|\mathcal{W}_k \odot \mathcal{Z}_k\|_{2,1} + \langle \mathcal{B} \times_k \mathbf{D}_k - \mathcal{Z}_k, \mathcal{P}_k \rangle \right. \\ & \quad \left. + \frac{\beta}{2} \|\mathcal{B} \times_k \mathbf{D}_k - \mathcal{Z}_k\|_F^2 \right\} + \frac{\rho}{2} \|\mathcal{B} - \mathcal{B}^l\|_F^2 \end{aligned} \quad (11)$$

where  $\mathcal{P}_k$  ( $k = 1, 2$ ) are the Lagrange multipliers and  $\beta > 0$  is the penalty parameter. To solve (10), we can alternately update  $\mathcal{B}$ ,  $\mathcal{Z}_k$ , and  $\mathcal{P}_k$  as

$$\begin{cases} \mathcal{B}^{l+1, p+1} = \underset{\mathcal{B}}{\text{argmin}} L_\beta(\mathcal{B}, \mathcal{Z}_k^p, \mathcal{P}_k^p) \\ \mathcal{Z}_k^{p+1} = \underset{\mathcal{Z}_k}{\text{argmin}} L_\beta(\mathcal{B}^{l+1, p+1}, \mathcal{Z}_k, \mathcal{P}_k^p) \\ \mathcal{P}_k^{p+1} = \mathcal{P}_k^p + \beta(\mathcal{B}^{l+1, p+1} \times_k \mathbf{D}_k - \mathcal{Z}_k^{p+1}). \end{cases} \quad (12)$$

Next, we solve  $\mathcal{B}^{l+1, p+1}$  and  $\mathcal{Z}_k^{p+1}$  in (12), respectively. For  $\mathcal{B}^{l+1, p+1}$ , we solve the following problem:

$$\begin{aligned} \underset{\mathcal{B}}{\text{argmin}} \quad & \frac{1}{2} \|\mathcal{Y} - \mathcal{B} \times_3 \mathbf{A}^{l+1} - \mathcal{S}^l\|_F^2 + \frac{\rho}{2} \|\mathcal{B} - \mathcal{B}^l\|_F^2 \\ & + \sum_{k=1}^2 \frac{\beta}{2} \left\| \mathcal{B} \times_k \mathbf{D}_k - \mathcal{Z}_k^p + \frac{\mathcal{P}_k^p}{\beta} \right\|_F^2 \end{aligned} \quad (13)$$

which can be directly solved by the following equation:

$$\mathcal{B} \times_3 ((\mathbf{A}^{l+1})^T \mathbf{A}^{l+1}) + \sum_{k=1}^2 \beta \mathcal{B} \times_k (\mathbf{D}_k^T \mathbf{D}_k) + \rho \mathcal{B} = \mathcal{K} \quad (14)$$

where

$$\begin{aligned} \mathcal{K} &= (\mathcal{Y} - \mathcal{S}^l) \times_3 (\mathbf{A}^{l+1})^T \\ & + \sum_{k=1}^2 \beta \left( \mathcal{Z}_k^p - \frac{\mathcal{P}_k^p}{\beta} \right) \times_k \mathbf{D}_k^T + \rho \mathcal{B}^l. \end{aligned}$$

<sup>3</sup> $\text{ones}(m, n)$  is an  $m \times n$  matrix whose elements are all 1.

Equation (14) can be equivalently rewritten as

$$\mathbf{B}_{(3)}^T ((\mathbf{A}^{l+1})^T \mathbf{A}^{l+1}) + \rho \mathbf{B}_{(3)}^T + \mathbf{C} \mathbf{B}_{(3)}^T = \mathbf{K}_{(3)}^T \quad (15)$$

where  $\mathbf{C} = \beta[(\mathbf{I}_{n_2} \otimes \mathbf{D}_1^T \mathbf{D}_1) + (\mathbf{D}_2^T \mathbf{D}_2 \otimes \mathbf{I}_{n_1})]$ . It is easy to find that the matrix  $\mathbf{C}$  has a structure of block circulant with circulant blocks, and the matrix  $(\mathbf{A}^{l+1})^T \mathbf{A}^{l+1}$  is a symmetric matrix. Thus, we employ 2-D FFT and SVD to diagonalize  $\mathbf{C}$  and  $(\mathbf{A}^{l+1})^T \mathbf{A}^{l+1}$ , respectively. That is

$$\mathbf{C} = \mathbf{F}_2^T \Psi_2 \mathbf{F}_2 \text{ and } (\mathbf{A}^{l+1})^T \mathbf{A}^{l+1} = \mathbf{U}_2 \Sigma_2 \mathbf{U}_2^T$$

where  $\mathbf{F}_2$  is 2-D DFT matrix. By using Theorem 1, we can efficiently solve (14) as

$$\mathcal{B}^{l+1, p+1} = \text{F}\circ\text{l}\text{d}_3\left([\mathbf{F}_2^T((1 \otimes \mathbf{T}_2) \odot (\mathbf{F}_2 \mathbf{K}_{(3)}^T \mathbf{U}_2)) \mathbf{U}_2^T]^T\right) \quad (16)$$

where

$$\begin{aligned} \mathbf{T}_2 &= (\text{diag}(\Psi_2), \text{diag}(\Psi_2), \dots, \text{diag}(\Psi_2)) + \rho \text{ones}(n_1 n_2, r) \\ & + (\text{diag}(\Sigma_2), \text{diag}(\Sigma_2), \dots, \text{diag}(\Sigma_2))^T. \end{aligned}$$

For  $\mathcal{Z}_k^{p+1}$  ( $k = 1, 2$ ), we solve the following problem:

$$\begin{aligned} \underset{\mathcal{Z}_k}{\text{argmin}} \quad & \tau \|\mathcal{W}_k \odot \mathcal{Z}_k\|_{2,1} \\ & + \frac{\beta}{2} \left\| \mathcal{B}^{k+1, p+1} \times_k \mathbf{D}_k - \mathcal{Z}_k + \frac{\mathcal{P}_k^p}{\beta} \right\|_F^2 \end{aligned} \quad (17)$$

which can be directly solved by

$$\mathcal{Z}_k^{p+1}(i, j, :) = \text{shrink}_{2,1}\left(\hat{\mathcal{Z}}_k(i, j, :), |\mathbf{W}_k(i, j)| \cdot \frac{\tau}{\beta}\right) \quad (18)$$

where

$$\begin{aligned} \hat{\mathcal{Z}}_k &= \mathcal{B}^{l+1, p+1} \times_k \mathbf{D}_k + \frac{\mathcal{P}_k^p}{\beta} \\ \mathbf{W}_k(i, j) &= \frac{1}{\|\hat{\mathcal{Z}}_k(i, j, :)\|_2 + \varepsilon} \\ \text{shrink}_{2,1}(\mathbf{x}, \xi) &= \begin{cases} \frac{\|\mathbf{x}\|_2 - \xi}{\|\mathbf{x}\|_2} \mathbf{x}, & \text{if } \xi < \|\mathbf{x}\|_2 \\ 0, & \text{otherwise} \end{cases} \end{aligned}$$

and  $\varepsilon$  is a small constant for avoiding the appearance of singularities.

3) *Update  $\mathcal{S}$ :* In Step 3 of (5), the  $\mathcal{S}$ -subproblem is as follows:

$$\begin{aligned} \underset{\mathcal{S}}{\text{argmin}} \quad & \frac{1}{2} \|\mathcal{Y} - \mathcal{B}^{l+1} \times_3 \mathbf{A}^{l+1} - \mathcal{S}^l\|_F^2 \\ & + \mu \|\mathcal{W}_s \odot \mathcal{S}\|_1 + \frac{\rho}{2} \|\mathcal{S} - \mathcal{S}^l\|_F^2 \end{aligned} \quad (19)$$

which has the following solution:

$$\mathcal{S}^{l+1} = \text{shrink}_1\left(\hat{\mathcal{S}}, \mathcal{W}_s \odot \frac{\mu}{1 + \rho}\right) \quad (20)$$

where

$$\hat{\mathcal{S}} = \frac{\mathcal{Y} - \mathcal{B}^{l+1} \times_3 \mathbf{A}^{l+1} + \rho \mathcal{S}^l}{1 + \rho}$$

$$\mathcal{W}_s(i, j, m) = \frac{1}{|\hat{\mathcal{S}}(i, j, m)| + \varepsilon}$$

and

$$[\text{shrink}_1(\mathcal{X}, \xi)]_{i,j,m} = \text{sign}(x_{i,j,m}) \max(|x_{i,j,m}| - \xi, 0).$$

**Algorithm 1** PAM-Based Solver for the LRTF-DFR-Based HSI Restoration Model

---

**Input:** The degraded observation HSI  $\mathcal{Y} \in \mathbb{R}^{n_1 \times n_2 \times n_3}$ , rank  $r$ , parameters  $\tau, \lambda, \mu, \beta$ , and  $\rho = 0.1$ .

**Initialization:**  $l = 0$ ,  $l_{\max} = 50$ ,  $p_{\max} = 10$ ,  $\mathbf{A}^0 = \text{rand}(n_3, r)$ ,  $\mathcal{B}^0 = \text{rand}(n_1, n_2, r)$ , and  $\mathcal{S}^0 = 0$ .

- 1: **while** not converged and  $l < l_{\max}$  **do**
- 2:   Update  $\mathbf{A}^{l+1}$  via (8).
- 3:   **Initialization:**  $p = 0$ ,  $\mathcal{Z}_k^0 = 0$  ( $k = 1, 2$ ), and  $\mathcal{P}_k^0 = 0$ .
- 4:   **while**  $p < p_{\max}$  **do**
- 5:     Update  $\mathcal{B}^{l+1, p+1}$  via (16).
- 6:     Update  $\mathcal{Z}_k^{p+1}$  via (18),  $k = 1, 2$ .
- 7:     Update  $\mathcal{P}_k^{p+1}$  via (12),  $k = 1, 2$ .
- 8:     Let  $p = p + 1$ .
- 9:     Check the convergence condition:  

$$\|\mathcal{B}^{l+1, p} - \mathcal{B}^{l+1, p-1}\|_F / \|\mathcal{B}^{l+1, p-1}\|_F < 10^{-4}$$
- 10:  **end while**
- 11:  Let  $\mathcal{B}^{l+1} = \mathcal{B}^{l+1, p}$ .
- 12:  Update  $\mathcal{S}^{l+1}$  via (20).
- 13:  Let  $l = l + 1$ .
- 14:  Check the convergence condition:  

$$\|\mathcal{B}^l \times_3 \mathbf{A}^l - \mathcal{B}^{l-1} \times_3 \mathbf{A}^{l-1}\|_F / \|\mathcal{B}^{l-1} \times_3 \mathbf{A}^{l-1}\|_F < 10^{-4}$$
- 15: **end while**

**Output:** The restored HSI  $\mathcal{X} = \mathcal{B} \times_3 \mathbf{A}$ .

---

By summarizing the aforementioned solving process, we describe the pseudocode of the developed PAM-based algorithm for solving the LRTF-DFR-based HSI restoration model in Algorithm 1.

#### D. Computational Complexity Analysis

We analyze the computational complexity of the developed PAM-based solving algorithm on a degraded HSI  $\mathcal{Y} \in \mathbb{R}^{n_1 \times n_2 \times n_3}$ . As shown in Algorithm 1, the computational cost at each outer iteration mainly lies in the updating of  $\mathbf{A}$ ,  $\mathcal{B}$ ,  $\mathcal{Z}_k$ ,  $\mathcal{P}_k$ ,  $\mathcal{S}$ , and the number of inner iterations  $p$ , where  $k = 1, 2$ . First, updating  $\mathbf{A}$  via (8) involves SVD, 1-D FFT, and several matrix multiplications, which leads to  $\mathcal{O}(rn_1n_2n_3 + r^2n_3 + rn_3\log(n_3))$  cost. Second, updating  $\mathcal{B}$  via (16) needs  $\mathcal{O}((r + n_1 + n_2)n_1n_2n_3 + r^2n_3 + rn_1n_2\log(n_1n_2))$  cost since it involves SVD, 2-D FFT, and several tensor-matrix product operations. Third, the computational cost of updating  $\mathcal{Z}_k$  ( $k = 1, 2$ ) via (18) is  $\mathcal{O}(n_1n_2n_3)$ . Fourth, the computational cost of updating  $\mathcal{P}_k$  via (12) is  $\mathcal{O}(n_1^2n_2r)$ . Finally, the computational cost of updating  $\mathcal{S}$  via (20) is  $\mathcal{O}(n_1n_2n_3)$ . In summary, the computational cost at each outer iteration of the developed PAM-based algorithm is  $\mathcal{O}(rn_3\log(n_3) + p((r + n_1 + n_2)n_1n_2n_3 + rn_1n_2\log(n_1n_2)))$ .

## IV. NUMERICAL EXPERIMENTS

We test the performance of the proposed LRTF-DFR-based HSI restoration method<sup>4</sup> by conducting extensive experiments

<sup>4</sup>The code of the proposed LRTF-DFR-based HSI restoration method is available at [https://github.com/YuBangZheng/code\\_LRTFDFR](https://github.com/YuBangZheng/code_LRTFDFR).

on both simulated and real HSIs. To comprehensively evaluate the proposed method, we compare five excellent HSI restoration methods, i.e., LRMR [35], NMoG [39], SNLRSF [56], LRTDTV [52], and LRTDGS [53]. We select LRMR and NMoG since they represent the classic methods based on matrix rank minimization and noise modeling, respectively. We select SNLRSF, LRTDTV, and LRTDGS since they are the most relevant to the proposed method among the newer methods for mixed noise removal. The detailed relations and distinctions between the proposed method and the compared methods are summarized in Table II.

All parameters involved in the compared methods are carefully adjusted based on the authors' suggestions in their articles to obtain the optimal performance. The gray values of HSIs are normalized into the interval [0, 1] band-by-band. All experiments are implemented by using MATLAB (R2019a) on Windows 10 with an Intel Core i9-9900K 3.60-GHz processor and 32-GB RAM.

#### A. Simulated Data Experiments

We employ two public HSIs in this section: one is the simulated Indian Pines data set<sup>5</sup> with the size of (145, 145, 224), which is also used in the compared methods LRTDTV and LRTDGS; the other is the Washington DC Mall data set<sup>6</sup> with the size of (256, 256, 191), which is also used in the compared methods LRMR, NMoG, SNLRSF, and LRTDGS. Three quantitative evaluation indexes, including the mean of peak signal-to-noise rate (MPSNR) over all bands, the mean of structural similarity (MSSIM) over all bands, and the mean of spectral angle mapping (MSAM) over all spectral vectors, are selected to evaluate the overall quality of the restored results quantitatively. Since the noise in HSIs usually manifests as a mixture of several kinds of noise in real noise scenarios, we consider the following five cases.

*Case 1 (Gaussian Noise):* The Gaussian noise with zero mean is added to all bands, and the noise standard deviation in each band is randomly sampled from the interval [0.1, 0.2].

*Case 2 (Gaussian Noise + Salt and Pepper Noise):* The Gaussian noise is added in the same way as Case 1. Furthermore, the salt and pepper noise is added to all bands, and the noise proportion in each band is randomly sampled from the interval [0.1, 0.2].

*Case 3 (Gaussian Noise + Salt and Pepper Noise + Stripe):* The Gaussian noise and the salt and pepper noise are added in the same way as Case 2. Furthermore, 40% of all bands are randomly selected to add stripes, and the number of stripes in each selected band is randomly sampled from the set {6, 7, ..., 15}. Especially, all elements of the whole column will become a certain value randomly sampled from the interval [0.6, 0.8] if this column is selected to add the stripe.

*Case 4 (Gaussian Noise + Salt and Pepper Noise + Deadline):* The Gaussian noise and the salt and pepper noise are added in the same way as Case 2. Furthermore, 20% of all bands are randomly selected to add deadlines with the width of randomly sampled from the set [1, 2, 3], and the number

<sup>5</sup>This data set is generated in the same way as [49].

<sup>6</sup><http://lesun.weebly.com/hyperspectral-data-set.html>

TABLE II  
DETAILED RELATIONS AND DISTINCTIONS BETWEEN THE PROPOSED METHOD AND THE COMPARED METHODS

Method	Low-rankness			Local continuity			Nonlocal self-similarity			Group sparsity of SpatDIs	Noise assumption
	spatial	spectral	both	spatial	spectral	both	spatial	spectral	both		
LRMR	<input checked="" type="checkbox"/>			—			—			—	Gaussian and Laplace distributions
	minimizing the matrix rank			—			—				
NMoG	<input checked="" type="checkbox"/>			—			—			—	non-i.i.d. mixture of Gaussian distributions
	LRMF			—			—				
SNLRSF	<input checked="" type="checkbox"/>			—			<input checked="" type="checkbox"/> nonlocal low-rank regularization on factor			—	Gaussian and Laplace distributions
	subspace representation			—			—				
LRTDTV	<input checked="" type="checkbox"/>			—			—			—	Gaussian and Laplace distributions
	LRTD			spatial-spectral TV			—				
LRTDGS	<input checked="" type="checkbox"/>			<input checked="" type="checkbox"/> weighted $\ell_{2,1}$ -norm on SpatDIs of HSIs			—			weighted $\ell_{2,1}$ -norm on SpatDIs of HSIs	Gaussian and Laplace distributions
	LRTD			—			—				
LRTF-DFR	<input checked="" type="checkbox"/>			double factor-based regularization			—			weighted $\ell_{2,1}$ -norm on SpatDIs of spatial factor	Gaussian and Laplace distributions
	LRTF			—			—				

TABLE III  
QUANTITATIVE COMPARISON OF ALL COMPARED METHODS FOR DIFFERENT DATA SETS AND CASES

Dataset	Case	Indexes	Noise	LRMR	NMoG	SNLRSF	LRTDTV	LRTDGS	LRTF-DFR
Indian Pines	Case 1	MPSNR	16.642	32.718	31.992	40.709	37.988	40.477	<b>43.935</b>
		MSSIM	0.2697	0.8682	0.8289	0.9875	0.9822	0.9918	<b>0.9971</b>
		MSAM	16.984	2.3167	2.6231	0.7881	1.1982	0.8877	<b>0.6132</b>
	Case 2	MPSNR	11.752	31.103	30.290	31.026	35.112	38.569	<b>41.403</b>
		MSSIM	0.1442	0.8292	0.7987	0.8644	0.9674	0.9865	<b>0.9965</b>
		MSAM	27.294	2.7518	3.1394	3.0024	1.6669	1.1046	<b>0.8490</b>
	Case 3	MPSNR	11.711	30.006	29.674	29.813	33.440	35.534	<b>39.165</b>
		MSSIM	0.1411	0.8225	0.7972	0.8577	0.9608	0.9758	<b>0.9951</b>
		MSAM	27.204	3.4053	3.4743	3.5800	2.1837	2.0246	<b>1.3131</b>
	Case 4	MPSNR	11.518	29.401	29.566	29.188	33.102	33.487	<b>38.739</b>
		MSSIM	0.1404	0.8808	0.7955	0.8416	0.9583	0.9490	<b>0.9938</b>
		MSAM	28.402	4.2670	3.7107	4.1584	2.4177	3.4266	<b>1.7831</b>
	Case 5	MPSNR	11.409	28.216	29.019	27.827	32.307	32.263	<b>37.948</b>
		MSSIM	0.1362	0.7913	0.7916	0.8286	0.9548	0.9343	<b>0.9942</b>
		MSAM	28.566	5.0425	4.1730	5.1917	2.8256	4.0121	<b>1.7715</b>
	Mean time (s)			—	25.971	99.320	20.014	102.18	73.057
Washington DC Mall	Case 1	MPSNR	16.658	31.771	33.744	<b>36.885</b>	32.574	34.167	35.686
		MSSIM	0.2915	0.9056	0.9376	<b>0.9698</b>	0.9135	0.9398	0.9585
		MSAM	42.481	10.340	9.4375	5.1332	6.2833	7.0713	<b>5.0720</b>
	Case 2	MPSNR	11.055	30.113	32.125	28.448	30.225	32.804	<b>34.626</b>
		MSSIM	0.1257	0.8760	0.9174	0.8788	0.8669	0.9220	<b>0.9493</b>
		MSAM	51.274	10.481	13.636	8.2613	7.4229	7.8837	<b>5.4400</b>
	Case 3	MPSNR	10.874	29.245	31.893	27.225	29.579	31.981	<b>34.464</b>
		MSSIM	0.1216	0.8642	0.9150	0.8549	0.8548	0.9158	<b>0.9477</b>
		MSAM	50.975	11.073	11.082	9.0752	7.7969	10.105	<b>5.7019</b>
	Case 4	MPSNR	11.071	29.772	32.083	28.654	30.019	32.565	<b>34.061</b>
		MSSIM	0.1245	0.8723	0.9210	0.8786	0.8654	0.9200	<b>0.9462</b>
		MSAM	51.653	11.004	11.632	8.6462	7.7726	8.4999	<b>5.9657</b>
	Case 5	MPSNR	10.863	28.858	31.918	27.515	29.545	31.859	<b>33.933</b>
		MSSIM	0.1201	0.8593	0.9221	0.8600	0.8508	0.9164	<b>0.9450</b>
		MSAM	51.462	11.752	8.6390	9.3490	8.0001	10.036	<b>6.3431</b>
	Mean time (s)			—	64.054	208.11	58.121	290.47	240.88

of deadlines in each selected band is randomly sampled from the set [6, 7, ..., 10]. Especially, all elements of the whole column will become zero if this column is selected to add the deadline.

**Case 5 (Gaussian Noise + Salt and Pepper Noise + Stripe + Deadline):** The Gaussian noise and the salt and pepper noise

are added in the same way as Case 2. Furthermore, stripes and deadlines are added in the same way as Cases 3 and 4, respectively.

1) *Quantitative Comparison:* We report the MPSNR, MSSIM, MSAM, and the mean time values obtained by all compared methods in Table III. Especially, we highlight

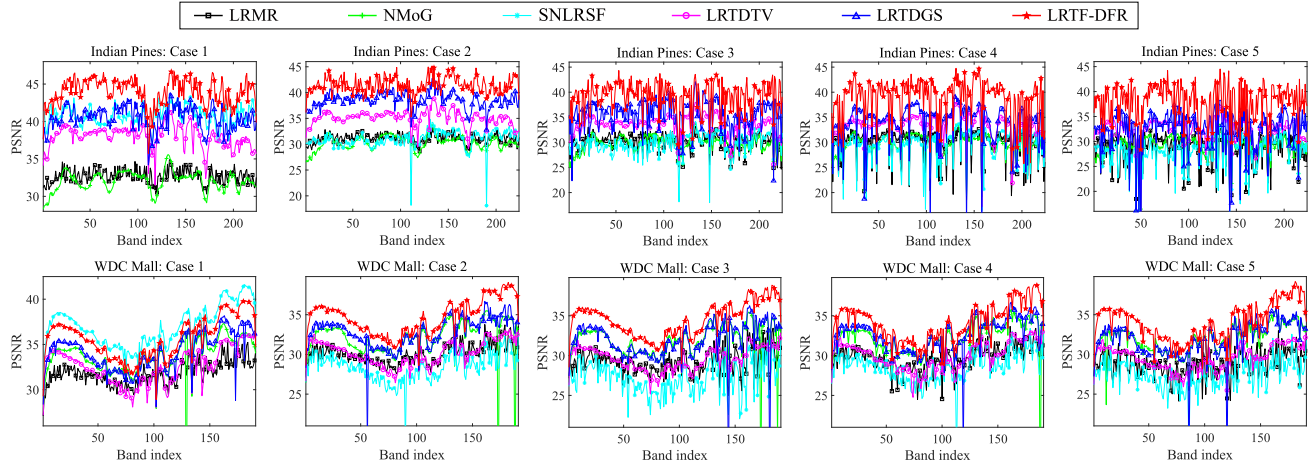


Fig. 3. PSNR values of all bands obtained by different compared methods under different cases. (From Left to Right) Results of cases 1–5, respectively. The first and the second rows are the results on HSIs Indian Pines and Washington DC Mall, respectively.

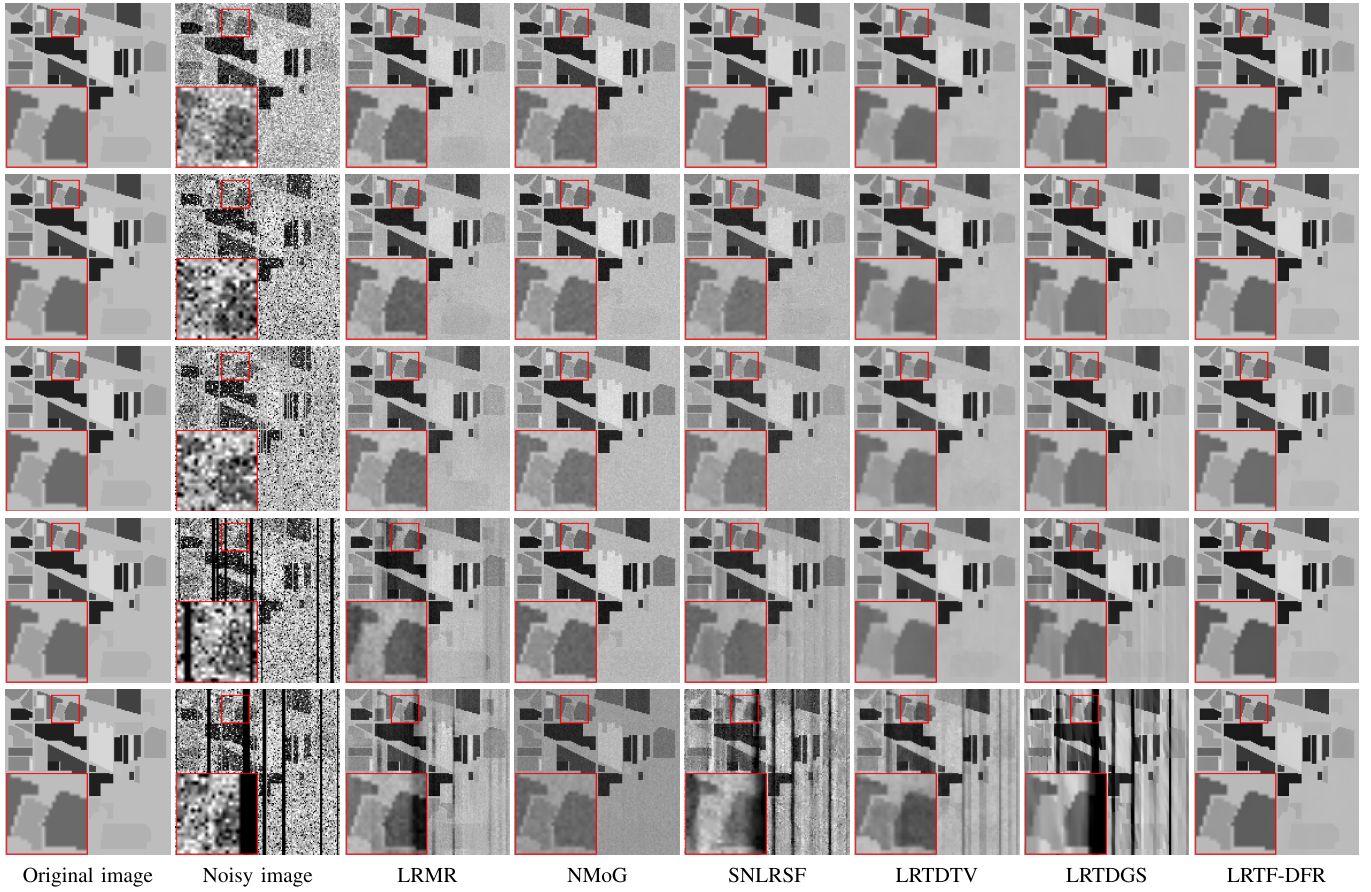


Fig. 4. Restoration results at band 48 of the Indian Pines data set. (From Top to Bottom) Results under cases 1–5, respectively. (From Left to Right) Original image, the noisy image, the results of LRMR, NMoG, SNLRSF, LRTDTV, LRTDGS, and LRTF-DFR, respectively.

the best results by bold. As observed, the proposed LRTF-DFR achieves overall superior results over the compared ones under nearly all cases. Although under case 1, SNLRSF outputs slightly higher MPSNR and MSSIM values than the proposed method on the Washington DC Mall data set, it obviously underperforms than the proposed method under other cases. For the running time, the proposed method costs

a shorter time than LRTDTV and LRTDGS. The main reason is that the proposed LRTF-DFR characterizes the HSI priors by introducing constraints on factors, while LRTDTV and LRTDGS by directly adding constraints on the original HSI. Meanwhile, the proposed method also costs a shorter time than NMoG with the reason that NMoG spends much time in noise learning. To compare the performance of each band, Fig. 3

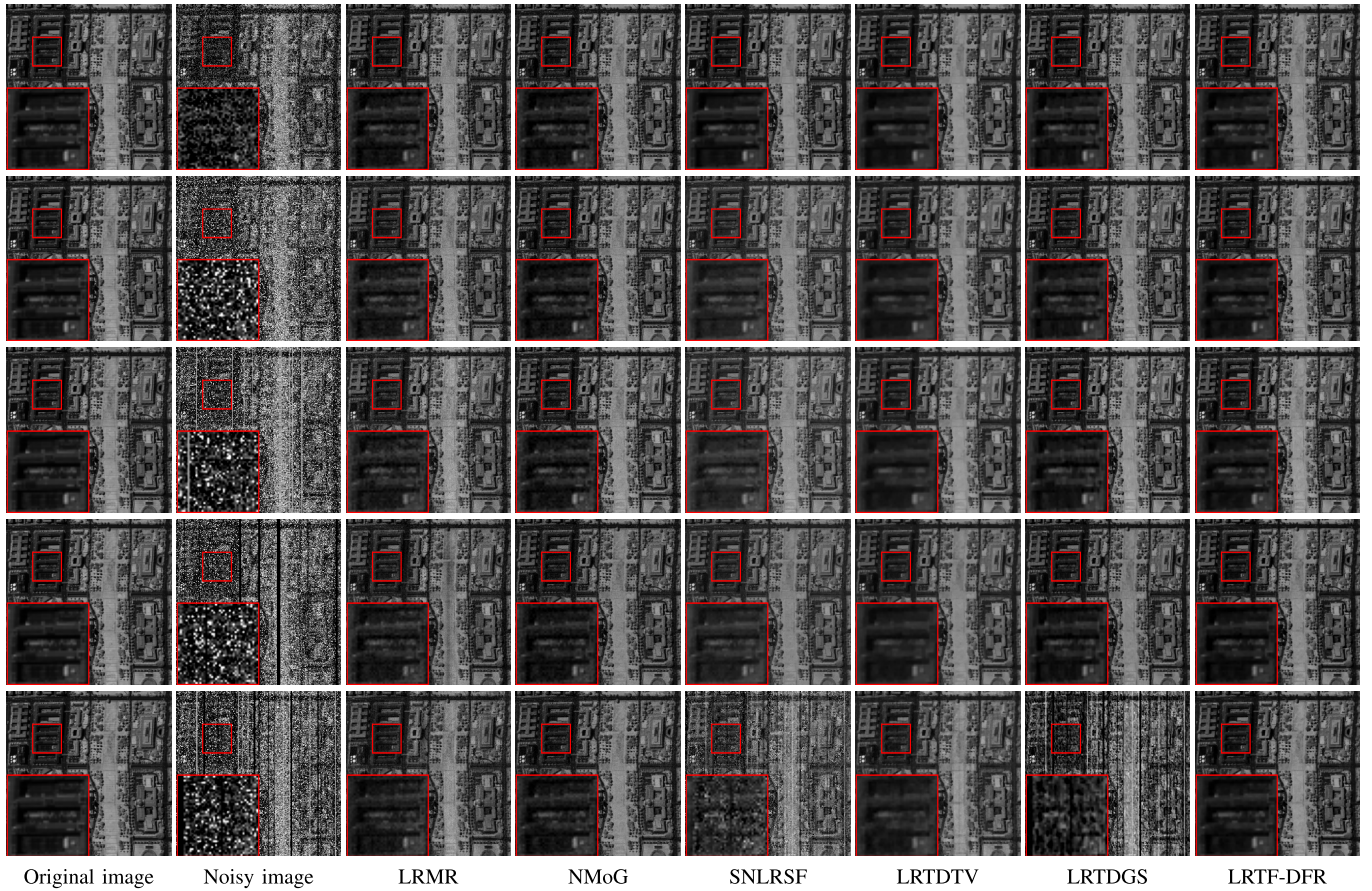


Fig. 5. Restoration results at band 86 of the Washington DC Mall data set. (From Top to Bottom) Results under cases 1–5, respectively. (From Left to Right) Original image, the noisy image, the results of LRMR, NMoG, SNLRSF, LRTDTV, LRTDGS, and LRTF-DFR, respectively.

shows the PSNR values of each band obtained by six compared methods. As observed, the proposed LRTF-DFR achieves the highest PSNR values among all the compared methods in most bands and cases.

2) *Qualitative Comparison*: To visually compare the restoration results, Fig. 4 shows band 48 of the Indian Pines data set restored by six compared methods under all cases. We observe from Fig. 4 that the proposed LRTF-DFR obtains the best visual results among all compared methods both in noise removal and the recovery of global structure and local details. Here LRMR, NMoG, and SNLRSF are not able to fully remove the noises, and LRTDTV and LRTDGS are not capable of well recovering the local details, especially the edges. Especially for case 5, the results of LRMR, SNLRSF, LRTDTV, and LRTDGS contain larger amounts of the trace of the thick deadlines. Comparatively, the proposed LRTF-DFR completely removes all noises while finely preserving the global structure and local details of the target HSI. Fig. 5 shows band 86 of the Washington DC Mall data set restored by six compared methods under all cases. It can be seen that the results of the proposed LRTF-DFR have an obvious improvement in noise removal and details preserving compared with the other methods.

To further compare the performance of the spectral curve recovery, cases 2 and 5 are selected as two representative cases. Fig. 6 shows the spectral curves at one spatial location of the restoration results by different compared methods under

cases 2 and 5. It is observed that the spectral curves obtained by the proposed LRTF-DFR can better approximate the original ones than those produced by the compared methods. In summary, the abovementioned observations illustrate that the proposed LRTF-DFR has the best performance on mixed noise removal, spatial image recovery, and spectral signatures preserving, among all compared methods.

The reason why the proposed LRTF-DFR is superior to the compared ones is that it can fully utilize the relevant information among different bands. More specifically, the proposed LRTF-DFR not only utilizes the global low rankness and the local continuity but also assumes that most of the smooth areas in different bands located at the same location, i.e., the SpatDI<sub>s</sub> of HSIs are group sparse along the spectral mode. This assumption makes the proposed LRTF-DFR to fully exploit the common characteristics among different bands. By contrast, LRMR, NMoG, and SNLRSF fail to consider the local continuity, LRTDTV does not consider the spectral group sparsity in the SpatDI<sub>s</sub>, and LRTDGS does not consider the local continuity in the spectral domain.

### B. Real Data Experiments

This section employs two real-world HSIs: one is the Urban data set<sup>6</sup> with a size of (307, 307, 210), which is also used in all compared methods; the other is the real Indian Pines data set<sup>6</sup> with a size of (145, 145, 220), which is also used in the compared methods SNLRSF, LRTDTV, and LRTDGS.

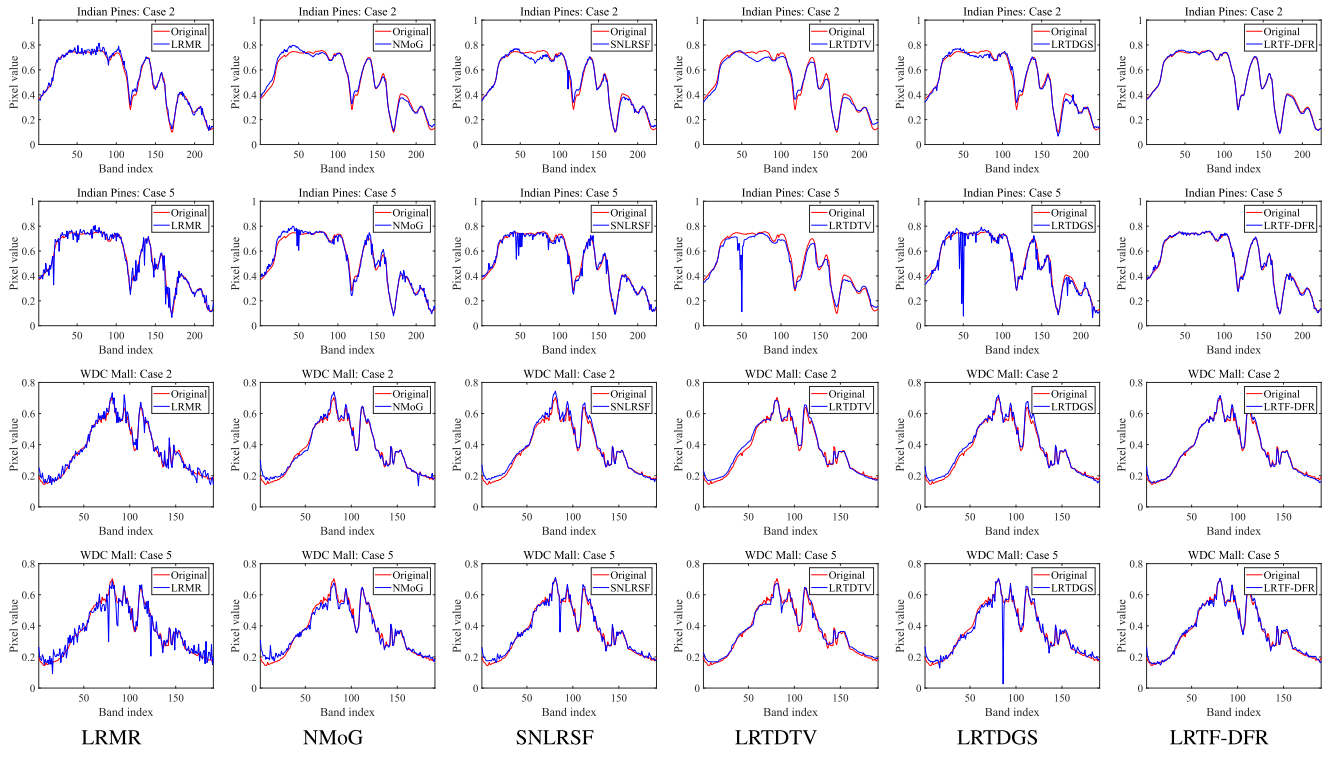


Fig. 6. Spectral curves of the restoration results by different compared methods. (From Left to Right) Results of LRMR, NMoG, SNLRSF, LRTDTV, LRTDGS, and LRTF-DFR, respectively. The first two rows are the results at spatial location (30, 30) of the Indian Pines data set under cases 2 and 5, respectively. The last two rows are the results at spatial location (151, 151) of the Washington DC Mall data set under cases 2 and 5, respectively.

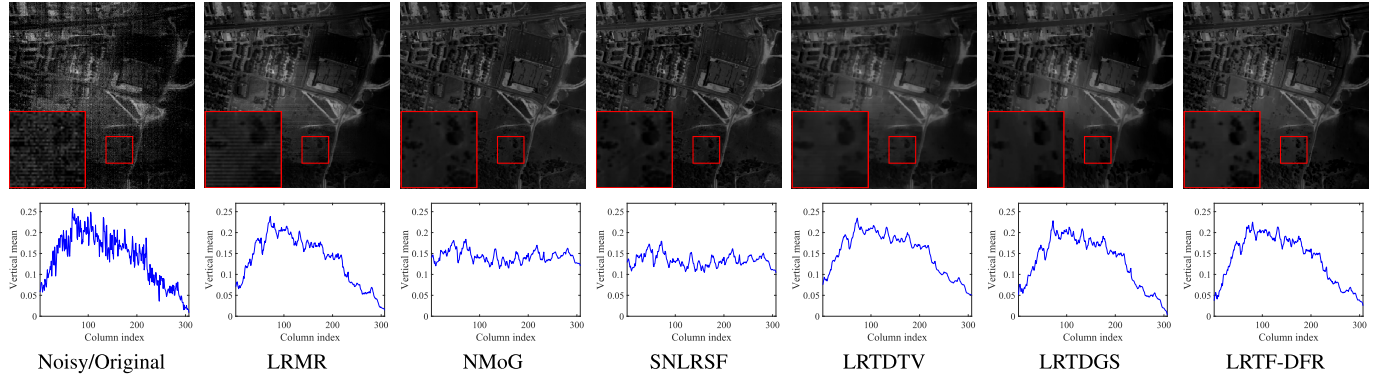


Fig. 7. Restoration results at band 109 of the real HSI Urban. (From Left to Right) Noisy/original result, the results of LRMR, NMoG, SNLRSF, LRTDTV, LRTDGS, and LRTF-DFR, respectively. The first and the second rows are the visual results and the vertical mean profiles, respectively.

**1) Urban Data Set:** Fig. 7 shows the restoration results at band 109 of the real HSI Urban, including the visual effects and the vertical mean profiles. Here, the vertical mean profile is a curve obtained by calculating the mean value of pixels in each column. As observed, all compared methods can effectively remove the mixed noise except LRMR, which cannot completely remove the stripes. However, by observing the enlarged box in Fig. 7, we can see that the results of LRTDTV and LRTDGS lose some local details. NMoG and SNLRSF have excellent ability to preserve the image details, whereas their vertical mean profiles deviate from the basic trend of the observed ones, implying the change of image contrast. Comparatively, the proposed LRTF-DFR completely

removes all noises, precisely preserves the global structure and local details, and finely retains the image contrast.

**2) Indian Pines Data Set:** Fig. 8 shows the restoration results at band 220 of the real HSI Indian Pines, including the visual effects and the vertical mean profiles. It is obvious that the result of LRMR contains a little noise; the reason is that LRMR only considers the low-rankness prior. NMoG, SNLRSF, LRTDTV, LRTDGS, and the proposed LRTF-DFR all have excellent ability to eliminate the noise and can produce relatively smooth vertical mean profiles. However, the proposed LRTF-DFR offers major advantages over the other ones for recovering local details, especially the edges.

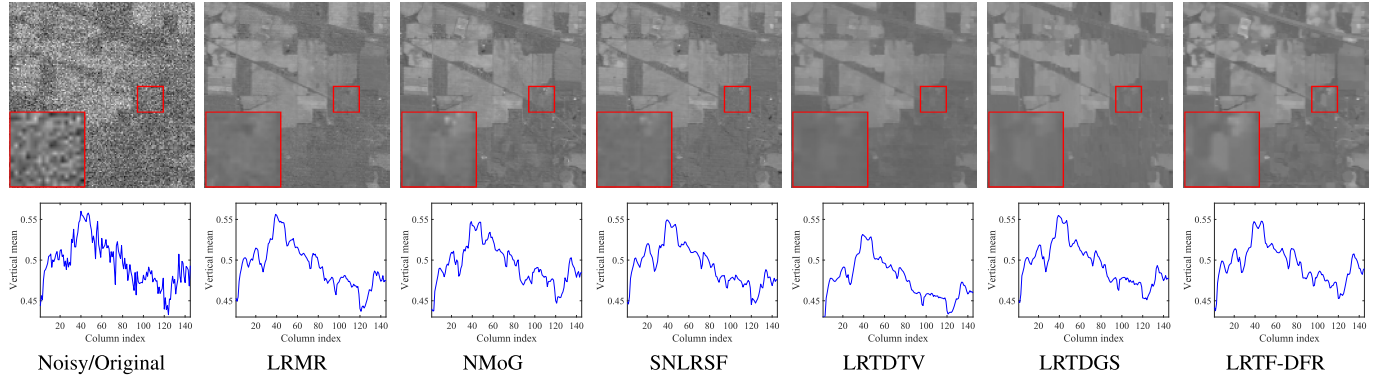


Fig. 8. Restoration results at band 220 of the real HSI Indian Pines. (From Left to Right) Noisy/original result, the results of LRMR, NMoG, SNLRSF, LRTDTV, LRTDGS, and LRTF-DFR, respectively. The first and the second rows are the visual results and the vertical mean profiles, respectively.

TABLE IV  
INFLUENCE OF THE NUMBER OF INNER ITERATION UNDER CASE 5 IN SIMULATED DATA EXPERIMENTS

Dataset	$p$	2	4	6	8	10	12	14	16	18	20
Indian Pines	MPSNR	33.284	36.354	37.146	37.541	37.986	38.112	38.148	38.152	38.178	38.184
	CPU time (s)	14.941	20.745	27.441	35.012	41.424	49.014	57.454	65.143	73.451	81.354
Washington DC Mall	MPSNR	33.210	33.547	33.697	33.821	33.921	33.924	33.931	33.942	33.956	33.961
	CPU time (s)	43.853	62.963	82.847	100.01	120.83	139.98	157.92	178.78	198.14	217.22

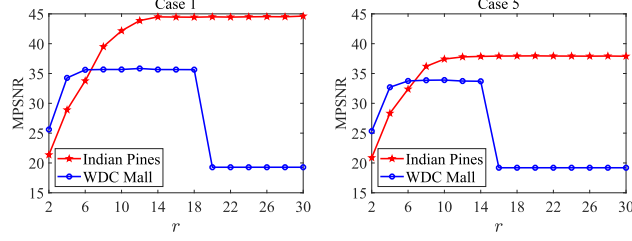


Fig. 9. Sensitivity analysis of the rank  $r$  under cases 1 and 5.

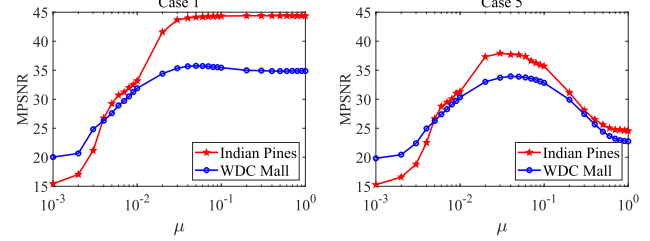


Fig. 11. Sensitivity analysis of the parameter  $\mu$  under cases 1 and 5.

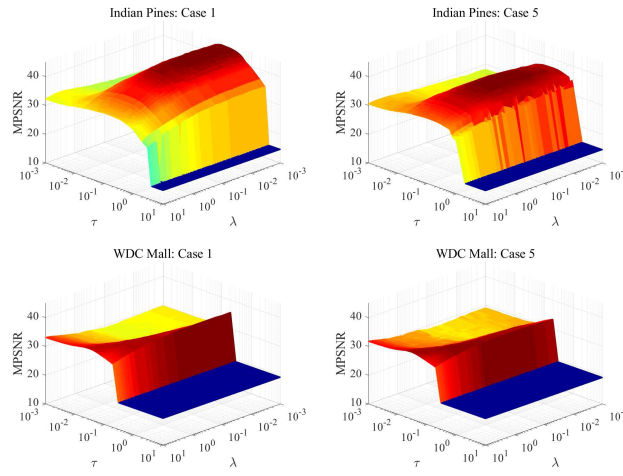


Fig. 10. Sensitivity analysis of the parameters  $\tau$  and  $\lambda$  under cases 1 and 5.

### C. Discussion

1) *Inner Iteration Analysis:* We test the influence of the number of inner iteration  $p$  on the simulated data sets under case 5. Table IV reports the MPSNR and CPU time values

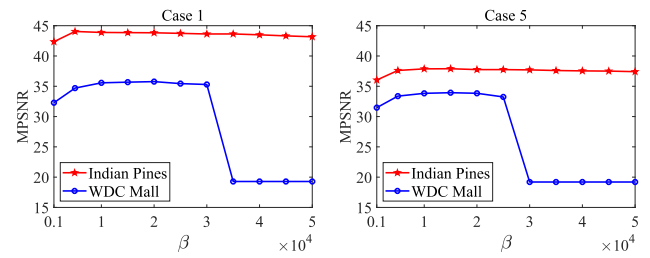


Fig. 12. Sensitivity analysis of the parameter  $\beta$  under cases 1 and 5.

with respect to different  $p$ 's. It is seen that the proposed LRTF-DFR obtains a stable and superior performance when  $p \geq 10$ . Considering that the CPU time is increased with increasing of  $p$ , we set  $p$  to be 10 in all experiments.

2) *Parameter Analysis:* We test the sensitivity of the parameters on the simulated data sets under cases 1 and 5 since they represent the Gaussian noise case and mixed noise case, respectively. As shown in Algorithm 1, the proposed LRTF-DFR method involves five important parameters: the rank  $r$ , regularization parameters  $\tau$ ,  $\lambda$ , and  $\mu$ , and the penalty parameter  $\beta$ .

TABLE V  
PARAMETERS SETTING OF THE PROPOSED LRTF-DFR IN SIMULATED DATA EXPERIMENTS

Dataset	$r$	$\tau$	$\lambda$	$\mu$	$\beta$
Indian Pines	12				
Washington DC Mall	8	0.2	0.01	0.04	15000

TABLE VI  
PARAMETERS SETTING OF THE PROPOSED LRTF-DFR IN REAL DATA EXPERIMENTS

Dataset	$r$	$\tau$	$\lambda$	$\mu$	$\beta$
Urban Indian Pines	Estimated by the HySime algorithm [62]	0.2	5	0.04	15000

The rank  $r$  mainly characterizes the spectral global correlation of HSIs. The sensitivity analysis of the rank  $r$  is presented in Fig. 9. It is seen that the proposed LRTF-DFR exhibits stable and superior performance within a certain range of the rank  $r$ . Considering that larger  $r$  leads to higher computational complexity, we set  $r$  to be 12 and 8 for the simulated Indian Pines data set and Washington DC Mall data set, respectively. Especially, the rank  $r$  is estimated by the well-known HySime algorithm [62] in real data experiments.

The parameters  $\tau$  and  $\lambda$  determine the weights of the factor  $\mathcal{B}$ -based and the factor  $\mathbf{A}$ -based regularization terms, respectively. Fig. 10 shows their sensitivity analysis. As observed, the performance of the proposed LRTF-DFR is robust to the parameter  $\lambda$ , while it is sensitive to the parameter  $\tau$ , especially in the Washington DC Mall data set. Moreover, as the parameters  $\tau$  and  $\lambda$  change, the MPSNR values have the same changing tendency for different noisy cases. This implies that these two parameters are robust to different noisy cases.

The parameter  $\mu$  determines the weight of the sparse noise term. Fig. 11 shows the sensitivity analysis of  $\mu$ . It is seen that the proposed LRTF-DFR has stable and superior performance under case 1 when  $\mu$  is larger than 0.04. This is because case 1 only involves the Gaussian noise. For case 5, the performance of LRTF-DFR is slightly sensitive to  $\mu$ , and the higher MPSNR values are achieved at  $\mu = 0.03, 0.04$ , and  $0.05$ .

The sensitivity analysis of the penalty parameter  $\beta$  is shown in Fig. 12. It is obvious that the performance of the proposed LRTF-DFR is robust within a certain range of  $\beta$ .

Under the guidance of the abovementioned analysis, Tables V and VI list the parameters setting of the proposed method in simulated data experiments and real data experiments, respectively.

3) *Convergence Analysis*: Since the ADMM and weighted strategies are embedded into the PAM framework, it is still an open problem for theoretically proving the convergence of the developed algorithm [57], [63]. Instead, we numerically demonstrate the convergence. Fig. 13 shows the relative change in the restored HSIs in each iteration and its previous iteration under cases 1 and 5. It is observed that for all testing data sets, the values of the relative change achieved by the developed algorithm monotonically decrease and gradually

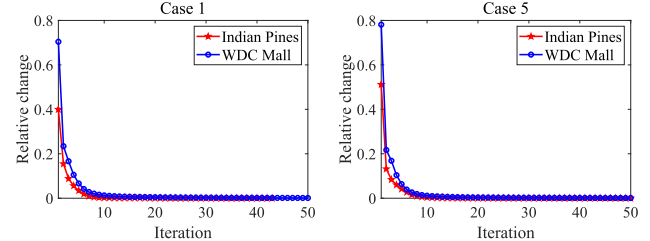


Fig. 13. Relative change curves with respect to the iteration number under cases 1 and 5.

tend to zeros, as the number of iterations increases. This justifies the strong convergence of the developed PAM-based solving algorithm numerically.

## V. CONCLUSION

In this article, we proposed an LRTF-DFR model for HSI mixed noise removal, which employed the LRTF framework to characterize the spectral global low rankness of HSIs, introduced a group sparsity constraint on the SpatDI of the spatial factor to promote the group sparsity in the SpatDI of HSIs, and suggested a continuity constraint on the spectral factor to promote the spectral continuity of HSIs. Especially, two weighted strategies are employed to better promote group sparsity and sparsity, respectively. To solve the proposed LRTF-DFR model, a PAM-based algorithm was developed with a numerically guaranteed convergence. By comparing with several excellent methods, including LRMR [35], NMoG [39], SNLRSF [56], LRTDTV [52], and LRTDGS [53], in extensive numerical experiments, the proposed method exhibited its superior performance on mixed noise removal, spatial image recovery, and spectral signatures preserving.

In the future, we will attempt to combine the proposed LRTF-DFR with the convolutional neural network [45], [64]–[66] to learn a more appropriate regularization on factors and further improve the ability of mixed noise removal.

## ACKNOWLEDGMENT

The authors would like to thank the editors and reviewers for their constructive comments, which are all valuable and helpful for improving this article. They would also like to thank the Medical Staff on the front line of fighting the COVID-19. It is their dedication and sacrifice that provide people a secure and stable research environment in this special time.

## REFERENCES

- [1] J. M. Bioucas-Dias *et al.*, “Hyperspectral unmixing overview: Geometrical, statistical, and sparse regression-based approaches,” *IEEE J. Sel. Topics Appl. Earth Observ. Remote Sens.*, vol. 5, no. 2, pp. 354–379, Apr. 2012.
- [2] H. Zhang, J. Li, Y. Huang, and L. Zhang, “A nonlocal weighted joint sparse representation classification method for hyperspectral imagery,” *IEEE J. Sel. Topics Appl. Earth Observ. Remote Sens.*, vol. 7, no. 6, pp. 2056–2065, Jun. 2014.
- [3] S. Prasad, D. Labate, M. Cui, and Y. Zhang, “Morphologically decoupled structured sparsity for rotation-invariant hyperspectral image analysis,” *IEEE Trans. Geosci. Remote Sens.*, vol. 55, no. 8, pp. 4355–4366, Aug. 2017.
- [4] S. Jia, L. Shen, J. Zhu, and Q. Li, “A 3-D Gabor phase-based coding and matching framework for hyperspectral imagery classification,” *IEEE Trans. Cybern.*, vol. 48, no. 4, pp. 1176–1188, Apr. 2018.

- [5] X. Fu, W.-K. Ma, T.-H. Chan, and J. M. Bioucas-Dias, "Self-dictionary sparse regression for hyperspectral unmixing: Greedy pursuit and pure pixel search are related," *IEEE J. Sel. Topics Signal Process.*, vol. 9, no. 6, pp. 1128–1141, Sep. 2015.
- [6] X. Fu, W.-K. Ma, J. M. Bioucas-Dias, and T.-H. Chan, "Semiblind hyperspectral unmixing in the presence of spectral library mismatches," *IEEE Trans. Geosci. Remote Sens.*, vol. 54, no. 9, pp. 5171–5184, Sep. 2016.
- [7] W. He, H. Zhang, and L. Zhang, "Total variation regularized reweighted sparse nonnegative matrix factorization for hyperspectral unmixing," *IEEE Trans. Geosci. Remote Sens.*, vol. 55, no. 7, pp. 3909–3921, Jul. 2017.
- [8] J. Li, X. Liu, Q. Yuan, H. Shen, and L. Zhang, "Antinoise hyperspectral image fusion by mining tensor low-multilinear-rank and variational properties," *IEEE Trans. Geosci. Remote Sens.*, vol. 57, no. 10, pp. 7832–7848, Oct. 2019.
- [9] Y. Liu, G. Gao, and Y. Gu, "Tensor matched subspace detector for hyperspectral target detection," *IEEE Trans. Geosci. Remote Sens.*, vol. 55, no. 4, pp. 1967–1974, Apr. 2017.
- [10] J. Li, Q. Yuan, H. Shen, and L. Zhang, "Noise removal from hyperspectral image with joint spectral-spatial distributed sparse representation," *IEEE Trans. Geosci. Remote Sens.*, vol. 54, no. 9, pp. 5425–5439, Sep. 2016.
- [11] X.-L. Zhao, W. Wang, T.-Y. Zeng, T.-Z. Huang, and M. K. Ng, "Total variation structured total least squares method for image restoration," *SIAM J. Sci. Comput.*, vol. 35, no. 6, pp. B1304–B1320, Jan. 2013.
- [12] X.-L. Zhao, F. Wang, and M. K. Ng, "A new convex optimization model for multiplicative noise and blur removal," *SIAM J. Imag. Sci.*, vol. 7, no. 1, pp. 456–475, Jan. 2014.
- [13] Y. Chang, L. Yan, H. Fang, and C. Luo, "Anisotropic spectral-spatial total variation model for multispectral remote sensing image destriping," *IEEE Trans. Image Process.*, vol. 24, no. 6, pp. 1852–1866, Jun. 2015.
- [14] T.-X. Jiang, T.-Z. Huang, X.-L. Zhao, and L.-J. Deng, "Multi-dimensional imaging data recovery via minimizing the partial sum of tubal nuclear norm," *J. Comput. Appl. Math.*, vol. 372, Jul. 2020, Art. no. 112680, doi: [10.1016/j.cam.2019.112680](https://doi.org/10.1016/j.cam.2019.112680).
- [15] M. Ding, T.-Z. Huang, T.-Y. Ji, X.-L. Zhao, and J.-H. Yang, "Low-rank tensor completion using matrix factorization based on tensor train rank and total variation," *J. Sci. Comput.*, vol. 81, no. 2, pp. 941–964, Nov. 2019.
- [16] Q. Xie, Q. Zhao, D. Meng, and Z. Xu, "Kronecker-basis-representation based tensor sparsity and its applications to tensor recovery," *IEEE Trans. Pattern Anal. Mach. Intell.*, vol. 40, no. 8, pp. 1888–1902, Aug. 2018.
- [17] J.-H. Yang, X.-L. Zhao, T.-Y. Ji, T.-H. Ma, and T.-Z. Huang, "Low-rank tensor train for tensor robust principal component analysis," *Appl. Math. Comput.*, vol. 367, Feb. 2020, Art. no. 124783.
- [18] W. He, N. Yokoya, L. Yuan, and Q. Zhao, "Remote sensing image reconstruction using tensor ring completion and total variation," *IEEE Trans. Geosci. Remote Sens.*, vol. 57, no. 11, pp. 8998–9009, Nov. 2019.
- [19] Q. Yao, J. T. Kwok, T. Wang, and T.-Y. Liu, "Large-scale low-rank matrix learning with nonconvex regularizers," *IEEE Trans. Pattern Anal. Mach. Intell.*, vol. 41, no. 11, pp. 2628–2643, Nov. 2019.
- [20] W. He, H. Zhang, H. Shen, and L. Zhang, "Hyperspectral image denoising using local low-rank matrix recovery and global spatial-spectral total variation," *IEEE J. Sel. Topics Appl. Earth Observ. Remote Sens.*, vol. 11, no. 3, pp. 713–729, Mar. 2018.
- [21] Y.-B. Zheng, T.-Z. Huang, T.-Y. Ji, X.-L. Zhao, T.-X. Jiang, and T.-H. Ma, "Low-rank tensor completion via smooth matrix factorization," *Appl. Math. Model.*, vol. 70, pp. 677–695, Jun. 2019.
- [22] J.-H. Yang, X.-L. Zhao, T.-H. Ma, Y. Chen, T.-Z. Huang, and M. Ding, "Remote sensing images destriping using unidirectional hybrid total variation and nonconvex low-rank regularization," *J. Comput. Appl. Math.*, vol. 363, pp. 124–144, Jan. 2020.
- [23] Q. Zhang, Q. Yuan, C. Zeng, X. Li, and Y. Wei, "Missing data reconstruction in remote sensing image with a unified Spatial-Temporal-Spectral deep convolutional neural network," *IEEE Trans. Geosci. Remote Sens.*, vol. 56, no. 8, pp. 4274–4288, Aug. 2018.
- [24] A. Buades, B. Coll, and J.-M. Morel, "A non-local algorithm for image denoising," in *Proc. IEEE Comput. Soc. Conf. Comput. Vis. Pattern Recognit. (CVPR)*, Jun. 2005, pp. 60–65.
- [25] M. Elad and M. Aharon, "Image denoising via sparse and redundant representations over learned dictionaries," *IEEE Trans. Image Process.*, vol. 15, no. 12, pp. 3736–3745, Dec. 2006.
- [26] K. Dabov, A. Foi, V. Katkovnik, and K. Egiazarian, "Image denoising by sparse 3-D transform-domain collaborative filtering," *IEEE Trans. Image Process.*, vol. 16, no. 8, pp. 2080–2095, Aug. 2007.
- [27] S. Gu, L. Zhang, W. Zuo, and X. Feng, "Weighted nuclear norm minimization with application to image denoising," in *Proc. IEEE Conf. Comput. Vis. Pattern Recognit.*, Jun. 2014, pp. 2862–2869.
- [28] Q. Yuan, L. Zhang, and H. Shen, "Hyperspectral image denoising employing a Spectral-Spatial adaptive total variation model," *IEEE Trans. Geosci. Remote Sens.*, vol. 50, no. 10, pp. 3660–3677, Oct. 2012.
- [29] G. Chen and S.-E. Qian, "Denoising of hyperspectral imagery using principal component analysis and wavelet shrinkage," *IEEE Trans. Geosci. Remote Sens.*, vol. 49, no. 3, pp. 973–980, Mar. 2011.
- [30] A. Danielyan, A. Foi, V. Katkovnik, and K. Egiazarian, "Denoising of multispectral images via nonlocal groupwise spectrum-PCA," in *Proc. Conf. Colour Graph., Imag., Vis.*, Jan. 2010, pp. 261–266.
- [31] Y. Peng, D. Meng, Z. Xu, C. Gao, Y. Yang, and B. Zhang, "Decomposable nonlocal tensor dictionary learning for multispectral image denoising," in *Proc. IEEE Conf. Comput. Vis. Pattern Recognit.*, Jun. 2014, pp. 2949–2956.
- [32] Y. Chen, W. He, N. Yokoya, T.-Z. Huang, and X.-L. Zhao, "Non-local tensor-ring decomposition for hyperspectral image denoising," *IEEE Trans. Geosci. Remote Sens.*, vol. 58, no. 2, pp. 1348–1362, Feb. 2020.
- [33] L. Zhuang and J. M. Bioucas-Dias, "Fast hyperspectral image denoising and inpainting based on low-rank and sparse representations," *IEEE J. Sel. Topics Appl. Earth Observ. Remote Sens.*, vol. 11, no. 3, pp. 730–742, Mar. 2018.
- [34] W. He, Q. Yao, C. Li, N. Yokoya, and Q. Zhao, "Non-local meets global: An integrated paradigm for hyperspectral denoising," in *Proc. IEEE/CVF Conf. Comput. Vis. Pattern Recognit. (CVPR)*, Jun. 2019, pp. 6868–6877.
- [35] H. Zhang, W. He, L. Zhang, H. Shen, and Q. Yuan, "Hyperspectral image restoration using low-rank matrix recovery," *IEEE Trans. Geosci. Remote Sens.*, vol. 52, no. 8, pp. 4729–4743, Aug. 2014.
- [36] Y. Xie, Y. Qu, D. Tao, W. Wu, Q. Yuan, and W. Zhang, "Hyperspectral image restoration via iteratively regularized weighted schatten  $p$ -Norm minimization," *IEEE Trans. Geosci. Remote Sens.*, vol. 54, no. 8, pp. 4642–4659, Aug. 2016.
- [37] Y. Chen, Y. Guo, Y. Wang, D. Wang, C. Peng, and G. He, "Denoising of hyperspectral images using nonconvex low rank matrix approximation," *IEEE Trans. Geosci. Remote Sens.*, vol. 55, no. 9, pp. 5366–5380, Sep. 2017.
- [38] X. Cao, Q. Zhao, D. Meng, Y. Chen, and Z. Xu, "Robust low-rank matrix factorization under general mixture noise distributions," *IEEE Trans. Image Process.*, vol. 25, no. 10, pp. 4677–4690, Oct. 2016.
- [39] Y. Chen, X. Cao, Q. Zhao, D. Meng, and Z. Xu, "Denoising hyperspectral image with non-i.i.d. Noise structure," *IEEE Trans. Cybern.*, vol. 48, no. 3, pp. 1054–1066, Mar. 2018.
- [40] N. Renard, S. Bourennane, and J. Blanc-Talon, "Denoising and dimensionality reduction using multilinear tools for hyperspectral images," *IEEE Geosci. Remote Sens. Lett.*, vol. 5, no. 2, pp. 138–142, Apr. 2008.
- [41] D. Letexier and S. Bourennane, "Noise removal from hyperspectral images by multidimensional filtering," *IEEE Trans. Geosci. Remote Sens.*, vol. 46, no. 7, pp. 2061–2069, Jul. 2008.
- [42] X. Liu, S. Bourennane, and C. Fossati, "Denoising of hyperspectral images using the PARAFAC model and statistical performance analysis," *IEEE Trans. Geosci. Remote Sens.*, vol. 50, no. 10, pp. 3717–3724, Oct. 2012.
- [43] H. Fan, Y. Chen, Y. Guo, H. Zhang, and G. Kuang, "Hyperspectral image restoration using low-rank tensor recovery," *IEEE J. Sel. Topics Appl. Earth Observ. Remote Sens.*, vol. 10, no. 10, pp. 4589–4604, Oct. 2017.
- [44] Y.-B. Zheng, T.-Z. Huang, X.-L. Zhao, T.-X. Jiang, T.-H. Ma, and T.-Y. Ji, "Mixed noise removal in hyperspectral image via low-fibered-rank regularization," *IEEE Trans. Geosci. Remote Sens.*, vol. 58, no. 1, pp. 734–749, Jan. 2020.
- [45] Y. Chang, L. Yan, H. Fang, S. Zhong, and W. Liao, "HSI-DeNet: Hyperspectral image restoration via convolutional neural network," *IEEE Trans. Geosci. Remote Sens.*, vol. 57, no. 2, pp. 667–682, Feb. 2019.
- [46] Q. Zhang, Q. Yuan, J. Li, X. Liu, H. Shen, and L. Zhang, "Hybrid noise removal in hyperspectral imagery with a spatial-spectral gradient network," *IEEE Trans. Geosci. Remote Sens.*, vol. 57, no. 10, pp. 7317–7329, Oct. 2019.
- [47] W. Dong, H. Wang, F. Wu, G. Shi, and X. Li, "Deep spatial-spectral representation learning for hyperspectral image denoising," *IEEE Trans. Comput. Imag.*, vol. 5, no. 4, pp. 635–648, Dec. 2019.

- [48] B. Lin, X. Tao, and J. Lu, "Hyperspectral image denoising via matrix factorization and deep prior regularization," *IEEE Trans. Image Process.*, vol. 29, pp. 565–578, 2020.
- [49] W. He, H. Zhang, L. Zhang, and H. Shen, "Total-variation-regularized low-rank matrix factorization for hyperspectral image restoration," *IEEE Trans. Geosci. Remote Sens.*, vol. 54, no. 1, pp. 178–188, Jan. 2016.
- [50] Q. Wang, Z. Wu, J. Jin, T. Wang, and Y. Shen, "Low rank constraint and spatial spectral total variation for hyperspectral image mixed denoising," *Signal Process.*, vol. 142, pp. 11–26, Jan. 2018.
- [51] H. Zhang, L. Liu, W. He, and L. Zhang, "Hyperspectral image denoising with total variation regularization and nonlocal low-rank tensor decomposition," *IEEE Trans. Geosci. Remote Sens.*, early access, Nov. 8, 2019, doi: [10.1109/TGRS.2019.2947333](https://doi.org/10.1109/TGRS.2019.2947333).
- [52] Y. Wang, J. Peng, Q. Zhao, Y. Leung, X.-L. Zhao, and D. Meng, "Hyperspectral image restoration via total variation regularized low-rank tensor decomposition," *IEEE J. Sel. Topics Appl. Earth Observ. Remote Sens.*, vol. 11, no. 4, pp. 1227–1243, Apr. 2018.
- [53] Y. Chen, W. He, N. Yokoya, and T.-Z. Huang, "Hyperspectral image restoration using weighted group sparsity-regularized low-rank tensor decomposition," *IEEE Trans. Cybern.*, early access, Sep. 2, 2019, doi: [10.1109/TCYB.2019.2936042](https://doi.org/10.1109/TCYB.2019.2936042).
- [54] H. K. Aggarwal and A. Majumdar, "Hyperspectral unmixing in the presence of mixed noise using joint-sparsity and total variation," *IEEE J. Sel. Topics Appl. Earth Observ. Remote Sens.*, vol. 9, no. 9, pp. 4257–4266, Sep. 2016.
- [55] Y. Chen, T.-Z. Huang, X.-L. Zhao, and L.-J. Deng, "Hyperspectral image restoration using framelet-regularized low-rank nonnegative matrix factorization," *Appl. Math. Model.*, vol. 63, pp. 128–147, Nov. 2018.
- [56] C. Cao, J. Yu, C. Zhou, K. Hu, F. Xiao, and X. Gao, "Hyperspectral image denoising via subspace-based nonlocal low-rank and sparse factorization," *IEEE J. Sel. Topics Appl. Earth Observ. Remote Sens.*, vol. 12, no. 3, pp. 973–988, Mar. 2019.
- [57] H. Attouch, J. Bolte, and B. F. Svaiter, "Convergence of descent methods for semi-algebraic and tame problems: Proximal algorithms, forward–backward splitting, and regularized Gauss–Seidel methods," *Math. Program.*, vol. 137, nos. 1–2, pp. 91–129, Feb. 2013.
- [58] T. G. Kolda and B. W. Bader, "Tensor decompositions and applications," *SIAM Rev.*, vol. 51, no. 3, pp. 455–500, Aug. 2009.
- [59] J. Peng, Q. Xie, Q. Zhao, Y. Wang, D. Meng, and Y. Leung, "Enhanced 3DTV regularization and its applications on hyper-spectral image denoising and compressed sensing," 2018, *arXiv:1809.06591*. [Online]. Available: <http://arxiv.org/abs/1809.06591>.
- [60] E. J. Candès, M. B. Wakin, and S. P. Boyd, "Enhancing sparsity by reweighted  $\ell_1$  minimization," *J. Fourier Anal. Appl.*, vol. 14, no. 5, pp. 877–905, 2008.
- [61] S. Boyd, "Distributed optimization and statistical learning via the alternating direction method of multipliers," *Found. Trends Mach. Learn.*, vol. 3, no. 1, pp. 1–122, 2010.
- [62] J. M. Bioucas-Dias and J. M. P. Nascimento, "Hyperspectral subspace identification," *IEEE Trans. Geosci. Remote Sens.*, vol. 46, no. 8, pp. 2435–2445, Aug. 2008.
- [63] J. Bolte, A. Daniilidis, A. Lewis, and M. Shiota, "Clarke subgradients of stratifiable functions," *SIAM J. Optim.*, vol. 18, no. 2, pp. 556–572, Jan. 2007.
- [64] K. Zhang, W. Zuo, S. Gu, and L. Zhang, "Learning deep CNN denoiser prior for image restoration," in *Proc. IEEE Conf. Comput. Vis. Pattern Recognit. (CVPR)*, Jul. 2017, pp. 2808–2817.
- [65] Q. Yuan, Q. Zhang, J. Li, H. Shen, and L. Zhang, "Hyperspectral image denoising employing a spatial-spectral deep residual convolutional neural network," *IEEE Trans. Geosci. Remote Sens.*, vol. 57, no. 2, pp. 1205–1218, Feb. 2019.
- [66] X.-L. Zhao, W.-H. Xu, T.-X. Jiang, Y. Wang, and M. K. Ng, "Deep plug-and-play prior for low-rank tensor completion," *Neurocomputing*, to be published, doi: [10.1016/j.neucom.2020.03.018](https://doi.org/10.1016/j.neucom.2020.03.018).



**Yu-Bang Zheng** (Student Member, IEEE) received the B.S. degree in information and computing science from the Anhui University of Finance and Economics, Bengbu, China, in 2017. He is pursuing the Ph.D. degree with the School of Mathematical Sciences, University of Electronic Science and Technology of China, Chengdu, China.

His research interests include sparse and low-rank modeling for high-dimensional image processing problems.



**Ting-Zhu Huang** received the B.S., M.S., and Ph.D. degrees in computational mathematics from the Department of Mathematics, Xi'an Jiaotong University, Xi'an, China.

He is a Professor with the School of Mathematical Sciences, University of Electronic Science and Technology of China, Chengdu, China. His research interests include scientific computation and applications, numerical algorithms for image processing, numerical linear algebra, preconditioning technologies, and matrix analysis with applications.

Dr. Huang is an Editor of the Scientific World Journal, Advances in Numerical Analysis, the Journal of Applied Mathematics, the Journal of Pure and Applied Mathematics: Advances in Applied Mathematics, and the Journal of Electronic Science and Technology, China.



**Xi-Le Zhao** received the M.S. and Ph.D. degrees from the University of Electronic Science and Technology of China (UESTC), Chengdu, China, in 2009 and 2012, respectively.

He is a Professor with the School of Mathematical Sciences, UESTC. His research interests include image processing, computer vision, and machine learning.



**Yong Chen** received the B.S. degree from the School of Science, East China University of Technology, Nanchang, China, in 2015. He is pursuing the Ph.D. degree with the School of Mathematical Sciences, University of Electronic Science and Technology of China, Chengdu, China.

From 2018 to 2019, he was a Research Intern with the Geoinformatics Unit, RIKEN Center for Advanced Intelligence Project, Tokyo, Japan. His research interests include remote sensing image processing, sparse optimization, and low-rank representation.



**Wei He** (Member, IEEE) received the B.S. degree from the School of Mathematics and Statistics, Wuhan University, Wuhan, China, in 2012, and the Ph.D. degree in surveying, mapping and remote sensing (LIESMARS) from Wuhan University in 2017.

He is a Researcher with the Geoinformatics Unit, RIKEN Center for Advanced Intelligence Project, Tokyo, Japan. His research interests include image quality improvement, remote sensing image processing, matrix/tensor analysis, and deep learning.